The Thesis committee for Salah Ahmad Al-Hadab
Certifies that this is the approved version of the following thesis:

Diffraction imaging of sediment drifts in the Canterbury Basin, New Zealand

APPROVED BY

SUPERVISING COMMITTEE:

Sergey Fomel, Supervisor

Paul Stoffa

Robert Tatham

Diffraction imaging of sediment drifts in the Canterbury Basin, New Zealand

by

Salah Ahmad Al-Hadab, B.S.

THESIS

Presented to the Faculty of the Graduate School of

The University of Texas at Austin

in Partial Fulfillment

of the Requirements

for the Degree of

Master of Science in Geological Sciences

THE UNIVERSITY OF TEXAS AT AUSTIN

December 2012

Dedicated to my parents.

Acknowledgments

I would like to thank my advisor Sergey Fomel for his guidance and support throughout the course of my Master's program. I learned so much from his knowledge, wisdom, and dedication to research. I also thank Karl Schleicher for sharing his knowledge and work experience, and for the helpful discussions. Thanks are due to Craig Fluthrope for providing the seismic dataset. I thank my committee Paul Stoffa and Robert Tatham for the corrections and suggestions that significantly improved this thesis. Special thanks are due to Saudi Aramco and the Jackson School for giving me the opportunity to obtain a higher education degree. I also thank Texas Advanced Computing Center for providing access to high performance computing machines by which I was able to complete numerical experiments. I thank my parents for their continuous support and confidence they bestowed upon me, and I also thank my wife who has been a source of encouragement and support. I also extend my thanks to friends and colleagues at UT.

Salah Ahmad Al-hadab

The University of Texas at Austin

December 2012

Diffraction imaging of sediment drifts in the Canterbury Basin, New Zealand

Salah Ahmad Al-Hadab, M.S.Geo.Sci.

The University of Texas at Austin, 2012

Supervisor: Sergey Fomel

Analysis of scattered, or diffraction energy (the seismic response of small-scale objects) in the seismic data from Canterbury Basin, New Zealand reveals additional geological information about depositional patterns in sedimentary deposits. Diffraction images from the seismic response for Canterbury Basin provide complementary interpretation tools to the conventional specular reflection images. To image diffractions for a dataset from Canterbury Basin, I take the following steps: First, I attenuate multiples using a surface multiple prediction algorithm to predict multiples and apply regularized nonstationary regression to adaptively subtract the predicted multiples. Next, I separate diffractions using the plane-wave destruction method. The plane-wave destruction method removes conventional reflected energy in order to enhance the diffracted energy. I then apply a velocity continuation method on diffraction data to estimate migration velocities and then migrate the data using Kirchhoff migration in the dip-angle-gather domain. The resultant conventional and diffraction images are improved images suitable for geological interpretation of prograding sediment drifts.

Table of Contents

List of Tables

List of Figures

Chapter 1

Introduction

The Canterbury Basin is located off the eastern coast of the South Island of New Zealand and is composed of prograding sediment drifts formed in the Neogene geological period. The sediment drifts overlay limestone formed in the Paleogene geological period. The prograding sediment accumulation was influenced by the proximity of the Canterbury Basin to the Alpine fault and a stable geostrophic oceanic current. The Alpine fault and the high frequency of stratigraphic sequences of the Canterbury Basin sediment drifts have been the subject of active geological research areas (Lu et al., 2003; Lu and Fulthorpe, 2004; Lu et al., 2005). High resolution seismic reflection profiles have revealed a number of details about the geometries of the structural sediment drifts in the Canterbury Basin.

Even more details about the sediment drifts can be realized by considering seismic diffraction energy, which is the seismic response of small-scale scattering objects (Klem-Musatov, 1994; Moser and Howard, 2008). Thus, small-scale faults or small buried objects are better located by diffraction energy than specular reflections. The diffraction section is an additional supportive image that reveals small geological features hidden in the conventional seismic images and can possibly give geologists an additional tool for more accurate structural interpretation of seismic data. Thus sediment drifts can potentially be explained more clearly by interpreting diffraction images. My research objective is to apply new and improved seismic data processing

techniques to separate diffractions from specular reflections and to produce two images: a diffraction image and an enhanced conventional specular reflection image. I achieve this objective using tools available in the Madagascar software package.

Madagascar is an open-source software package for analysis and processing of multidimensional seismic data and conducting reproducible computational experiments with seismic data (`http://www.ahay.org/`). Madagascar has routines that implement algorithms from newly published papers such as regularized nonstationary autoregression for adaptive subtraction (Fomel, 2009a), velocity continuation for migration velocity analysis (Fomel, 2003), and automatic velocity picking for stacking velocity analysis (Fomel, 2009b).

In Chapter 2 , I provide an overview of the geology of Canterbury Basin and the objective of the seismic survey of revealing the structural geometries of the prograding sediment drifts from the Neogene period of geological time line. Then, I describe the seismic reflection dataset (profile 12) and the the characteristics of the marine survey design. After that, I present the three fundamental conventional seismic data processing steps: deconvolution, stacking, and migration. I also discuss the secondary supplementary processing steps that enhance the results of the major core processes.

In Chapter 3, I focus on the task of attenuating the multiple energy present in the dataset. Multiple energy is considered coherent noise that obscures the primary signal and therefore is actively attenuated during the processing sequence in order to enhance the primary signal. I discuss and apply the surface-related multiple prediction algorithm (Dragoset and Jeričević, 1998) to predict these surface multiples. Then, I describe and apply the nonstationary adaptive subtraction by the shaping regular-

ization method to attenuate the multiple energy (Fomel, 2009a). The nonstationary shaping regularization method attempts to account for differences in amplitude and phase between the actual recorded multiples and the predicted multiples.

In Chapter 4, I study and apply the plane-wave destruction (PWD) method for reflection energy suppression (Fomel et al., 2007). The PWD method effectively predicts and suppresses smooth, laterally continuous events such as reflections and, therefore, makes diffraction separation feasible. I also demonstrate the PWD diffraction separation method on synthetic data. Also, DMO (dip move-out) is a necessary processing step to preserve seismic diffractions for diffraction imaging when applied to poststack data.

In Chapter 5, I apply a velocity continuation method (Fomel, 2003) on zero-offset diffraction data in order to estimate migration velocities. Velocity continuation produces several images of diffractions, each image created with different migration velocity functions. The integral-path method (Landa et al., 2006) is one technique that could be used to extract the image that focuses the diffractions into their apexes and defines their corresponding migration velocities (Burnett et al., 2011). I then use the computed migration velocity to produce both a conventional reflection image and a supplemental diffraction image using Kirchhoff migration in the dip-angle gather domain.

In conclusion, a summary of possible directions for future work is provided in Chapter 6. For example, Kirchhoff migration in the dip-angle gather domain makes diffraction separation in the image space domain attractive. Reflections and diffractions in the migrated dip-angle gathers have different geometrical characteristics and, therefore, can be effectively separated.

Chapter 2

Canterbury Basin Geology and Processing Overview

Canterbury Basin, New Zealand

Canterbury Basin is located offshore the eastern coast of the South Island of New Zealand between Otago Peninsula and Banks Peninsula (Figure 2.1). The basin underlies the present-day onshore Canterbury plain, shown by dashed-line in the map, and the offshore continental shelf. Deposition occured during the Neogene geological period which is divided into Miocene (5 - 23 millions years ago) geological epoch and Paleocene (5 to 2.5 million years ago) epoch (Lu et al., 2003). The sediments overlay limestones formed in Oligocene and Eocene geological epochs of Paleogene geological period. The sedimentation process in the basin was influenced by its proximity to the active Alpine fault.

The Alpine fault separates the Australian and Pacific plates (Figure 2.1) and is an active area of geological investigation to understand the origin of the Alpine fault and its influence on the deposition in the area (Lu et al., 2005). The Alpine fault is a dextral strike-slip fault, the plates along the fault are moving in horizontal motions both past and towards each other. The movement of the Pacific plate and the Australian plate against each other causes a compressional force and a thrust of Pacific plate under the Australian plate uplifting and creating the Southern Alps (Lu et al., 2005). Figure 2.2 depicts the historical formation of Onekakara, Kerkenodon and Otakou which were deposited during the transgressive, highstand, regressive phase

of the cycle caused by rifting and transgressive of alpine fault plate boundary (Lu et al., 2003). The Otakou group is where the sediments drifts occur in the Canterbury Basin.

Sediment drifts, or contourites, are defined as "sediments in relatively deep water, deposited or significantly reworked by a stable geostrophic current" (Faugres and Stow, 1993). It is been also recognized that drifts not only form in deep water (2000 m), but also form in mid water depth (300 - 2000), and shallow water depth (50-300 m, outer shelf/upper slope). Accumulations of sediment drifts can be recognized by accretionary bedding architecture, flow-elongate geometry, and along slope facies trends. The sediment drifts in the Canterbury basin formed at shelf depth 200 m and are 1000 m thick, aggraded towards the paleoshelf, and terminated along the strike (Figure 2.3).

Seismic Field Data

High resolution and multichannel seismic (MCS) 2D marine reflection data were acquired in January 2000 in the offshore Canterbury Basin, New Zealand, by The University of Texas Institute for Geophysics (UTIG) for the purpose of studying the high frequency depositional and stratigraphic sequences (Lu et al., 2003). The Canterbury Basin exhibits high rate of Neogene sediment accumulation combined with a stable tectonic setting. The acquisition survey was designed in particular to image Neogene depositional sequences and stratal geometries which represent sediment drifts.

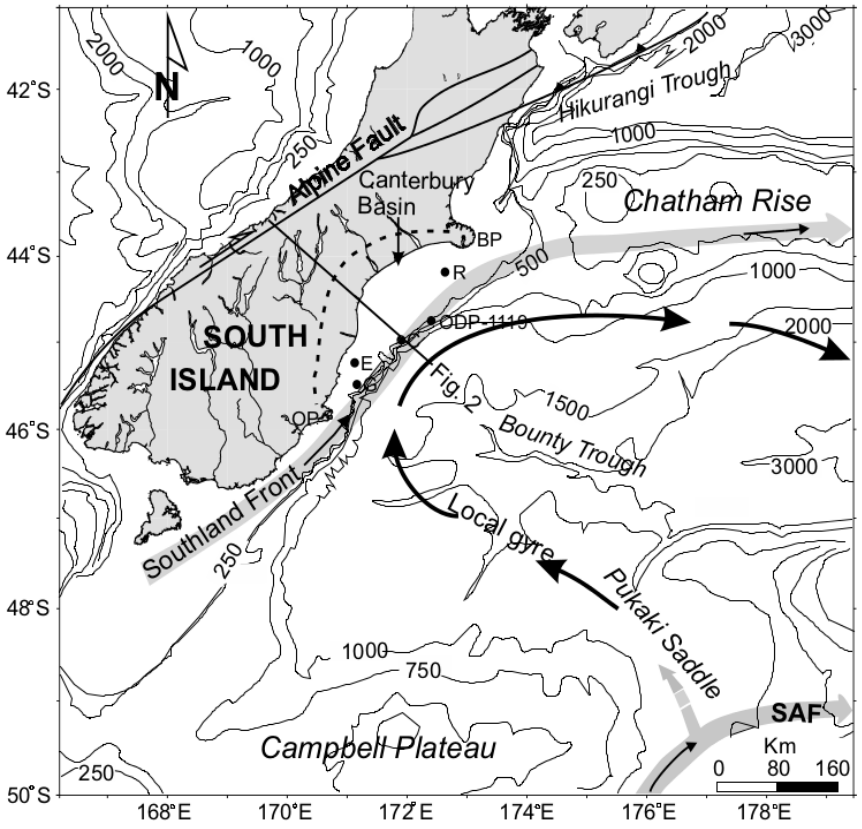

Figure 2.1: Location map showing the South Island of New Zealand. The Canterbury Basin underlies the present-day onshore Canterbury Plains and offshore continental shelf. It is bounded by the Miocene Volcanic centers of the Banks Peninsula (BP; 7.5-12 Ma) to the northeast and the Otago Peninsula (OP; 9.6-12.9 Ma) to the southwest, and faces the Bounty Trough to the southeast. the Alpine Fault is the dextral strike-slip boundary between the Australian and Pacific plates. Bathymetric contours are in meters. Figure from Lu et al. (2003).

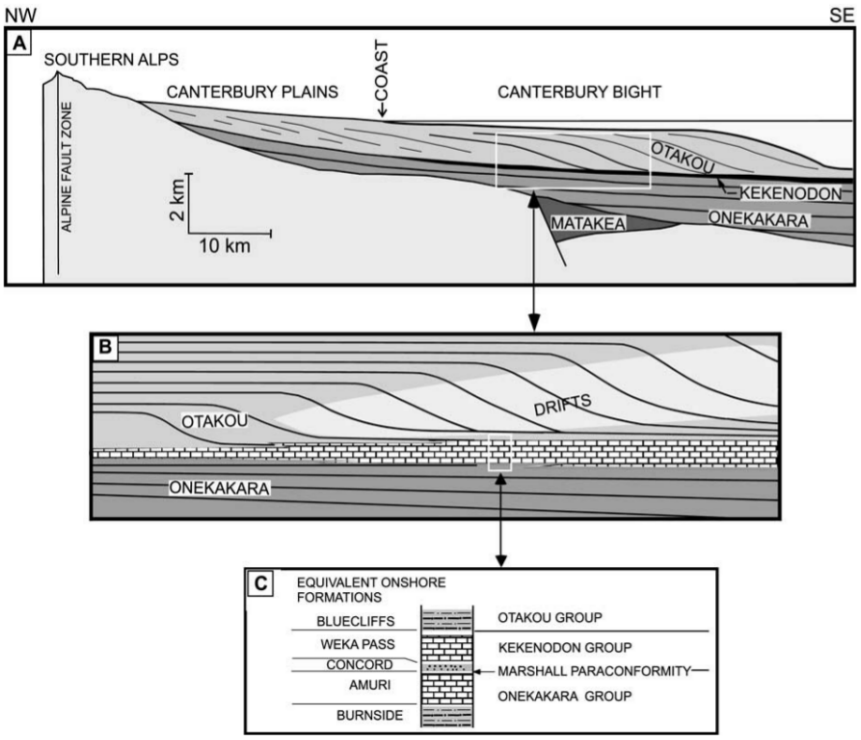

Figure 2.2: Schematic representing the stratigraphy of the Canterbury Basin at three scales. (A) Large scale, post-rift stratigraphy. Onekakara, Kekenodon and Otakou groups were deposited during regional transgressive, highstand and regressive phases, respectively. (B) Seismic-scale stratigraphy. The sediment drifts occur within the Otakou Group. The limestone are shown as distal facies of the uppermost transgressive Onekakara Groups and lowermost regressive Otakou Group. (C) Outcrop-scale stratigraphy across the Marchall Paraconformity. Figure from Lu et al. (2003).

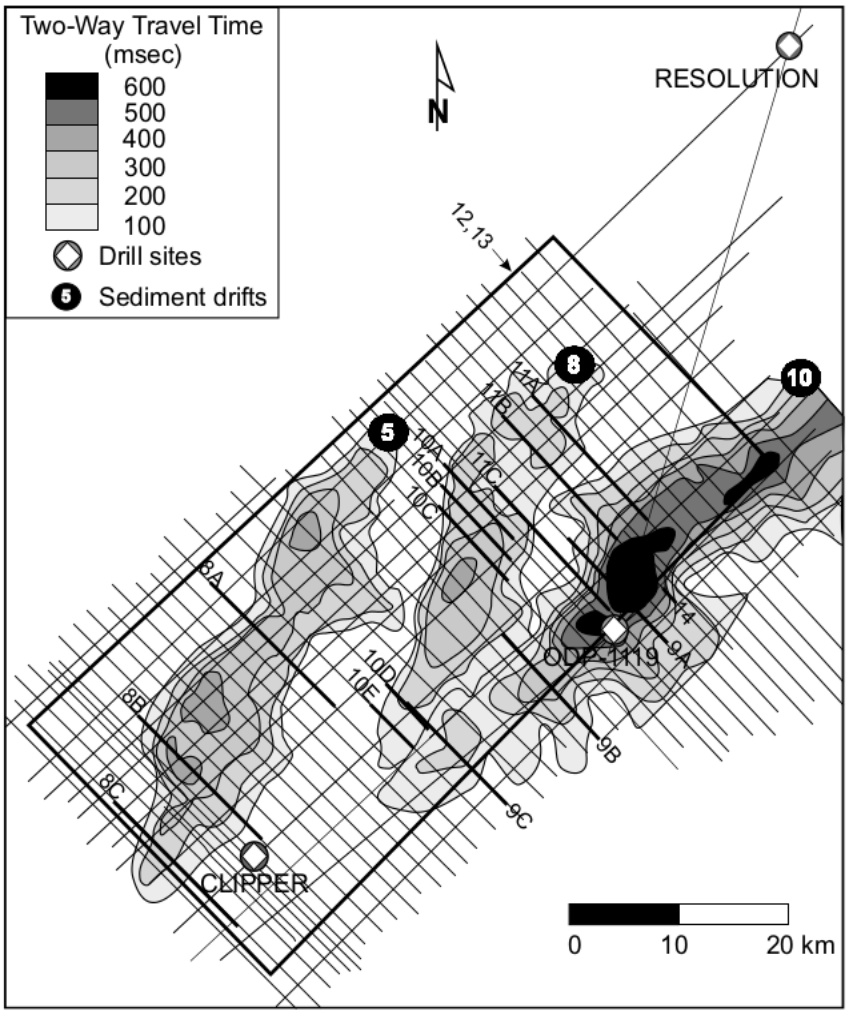

Figure 2.3: Isochron map (in ms two-way travel time) showing thickness of sediment drifts 5, 8, and 10. Drifts tend to be thick in the middle and thin along strike. Drift thickness, length, and width all increase northeastward across the basin and drift orientation becomes progressively more easterly. The location of seismic profiles 12 & 13 are indicated. Figure from Lu et al. (2003).

Seismic Profile 12 - Overview

Seismic Line 12 extends from southeast to northwest for the vessel streaming from SE to NW, and "shooting" updip towards the shore (Figure 2.3). The average slope of the sea floor is approximately 2°. The profile covers water depths varying from 150 m to 2400 m. Table 2.1 summarizes the acquisition parameters used for seismic line 12. Figure 2.4, reproduced from Claerbout (1985), depicts the recording geometry of typical marine streamers of 2D surveys, and illustrates the various "sorting", or "gathering" schemes often used in organizing common midpoint (CMP) seismic data. The lower diagram (stacking diagram) in the figure shows seismogram by dots. These dots may be grouped into several data gathering domains. For example, the common midpoint gather as shown in the diagram corresponds to seismograms recorded from one common midpoint (CMP); that is, the same physical midpoint location. Seismic line 12 was acquired with a shot interval equal to the receiver interval. This configuration of shot and receiver spacing results in two different near offsets for CMPs in the "gathered" records as illustrated in Figure 2.5. There are two different near offsets (distance from the shot to the first receiver). Odd number traces have the same near offset while the even numbered traces have a different near offset. This CMP gather geometry requires attention during seismic data processing. Improper consideration of these differences results in a stacked section with traces shifted up and down in the time as shown in Figure 2.6(b). This effect especially appears in the shallower, CMP fold, part of the CMP stacked section.

Seismic Profile 12 - Processing

Conventional data processing of reflection seismic data aims at producing a meaningful image of the subsurface structure, usually with the vertical axis in two-

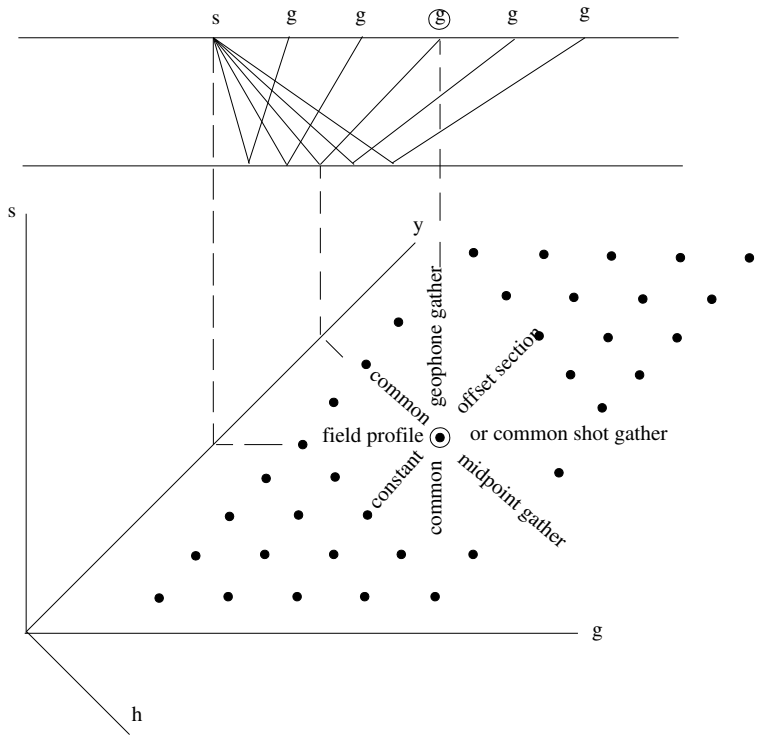

Figure 2.4: Profile (top) and stacking diagram (bottom) schematic of field recording of marine seismograms from a shot at location s to a hydrophone location labeled g. The lower diagram called a stacking_diagram and is not a prespective drawing, which illustrates various schemes of "gathering" the recorded traces. Each dot in this plane represents a single trace seismogram. The center hydrophone above (circled) records the seismogram (circled dot) that may be found in various geophysical displays or "gathering" schemes. Line in this (s,g)-plane are planes in the (t,s,g)-volume where t is the two-way traveltime associated with each trace. Planes of various orientations have the names discussed in the text. Figure from Claerbout (1985).

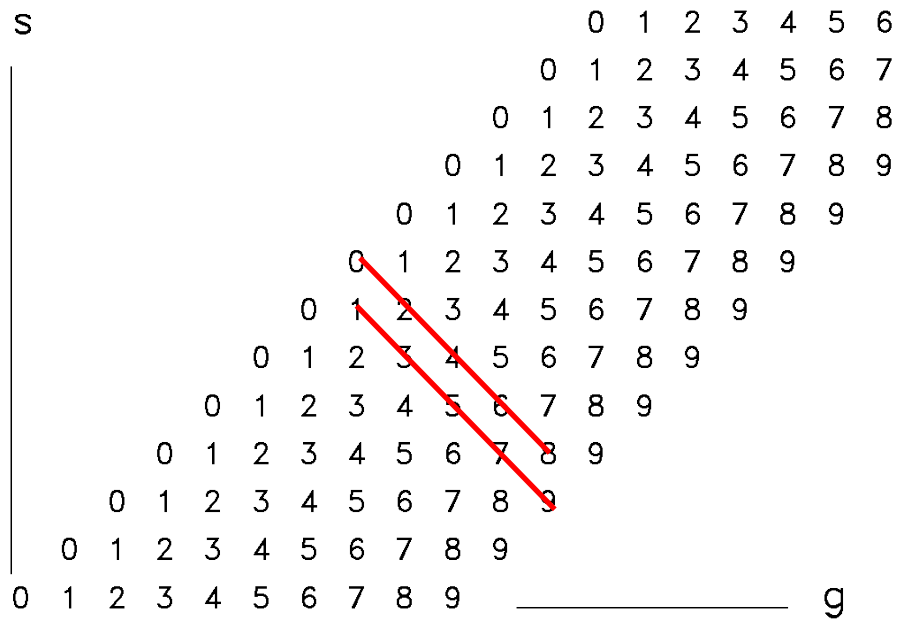

Figure 2.5: "stacking diagram" for Δg (receiver spacing)=Δs (shot spacing). The zero-offset section lies under the zeros. The CMP gathers of even numbered receivers and the CMPs composed of the odd numbered receivers have two different offset geometries. Thus there are two different kinds of CMP gathers, each kind has a different near-offset. Each of these CMP gathers have an offset interval of Δg. Figure from Claerbout (1985).

Source - 2 45/45 GI (generator-injector) airguns at 2000 psi	2.5 m depth
Shot interval	12.5 m
Receiver interval	12.5 m
Number of receiver groups	120
Near trace Offset	29.25 m
Far trace Offset	1516.75 m
CMP interval	6.25 m
Fold of coverage	60
Total number of CMPs	9701
Line (profile) length	58 km
Digital sampling interval	1 ms
Maximum recording time	3 s
Total data volume	7.9 GB

Table 2.1: Acquisition parameters for the Canterbury seismic data set of Line 12. Notice the high resolution of the acquired data both laterally and vertically.

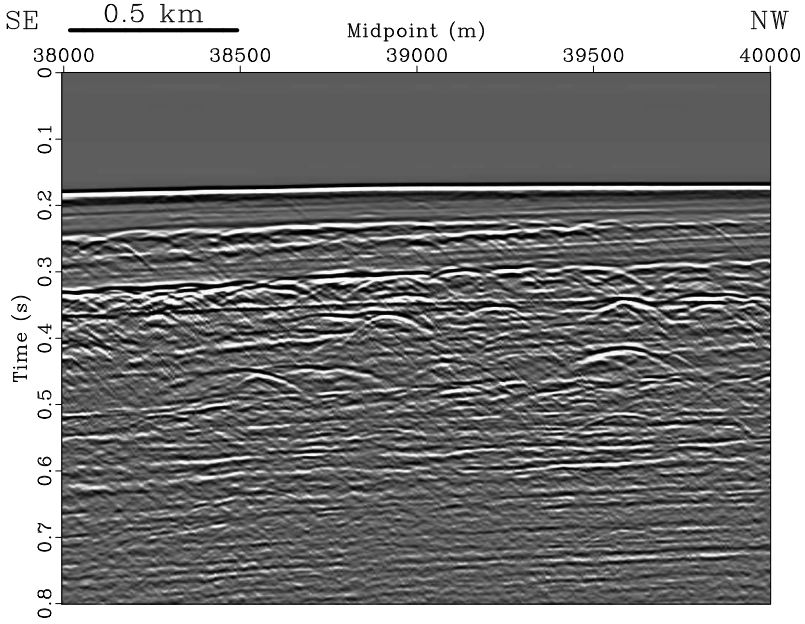

(a)

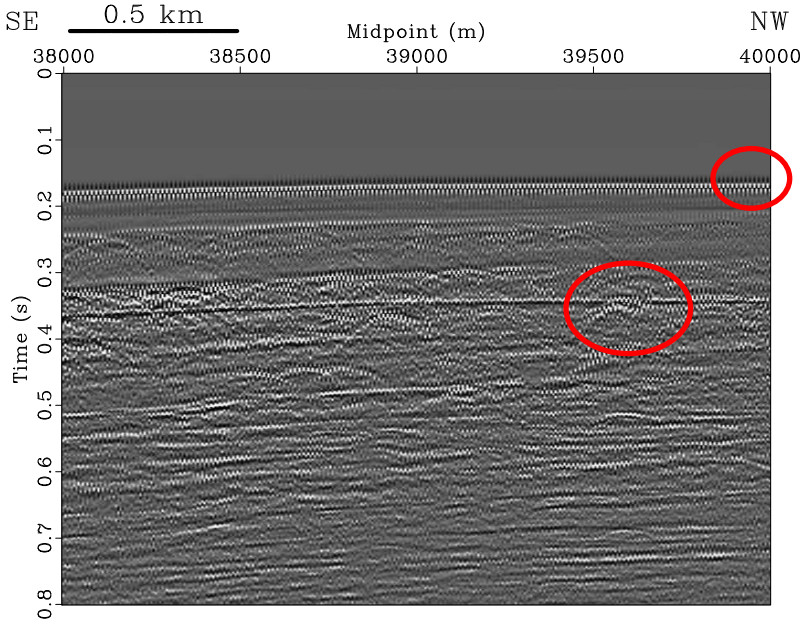

(b)

Figure 2.6: Good quality stack (a), and poor quality stack (b) resulting from improper handling of the two different near-offsets in the two types of CMP gathers. Note the periodic variation in mis-stack (circled) for the shallow water reflection in (b).

way traveltime (Yilmaz, 2001). After correction of the data for navigation and field effects, seismic data processing is frequencly focused on three major processing steps: deconvolution, stacking, and migration. The effectiveness of a major processing step is often enhanced by incorporating secondary procedures such as amplitude gain, trace editing, and bandpass filtering within each groups of processes.

Deconvolution is a time-series analysis technique applied along the time axis to each recorded trace to remove or compress the input source wavelet which is imposed on the data and, thus increase the temporal resolution. Predictive deconvolution is a popular technique that compresses the source wavelet and simultaneously removes short period reverbations due to shallow multiples or source bubble effects (Robinson and Treitel, 2000). Deconvolution requires assumptions such as statistical stationary and often a known source wavelet which are not strictly valid (Yilmaz, 2001). Nevertheless, the technique has been widely used in the industry and usually produces satisfactory results.

With the assumption of a random reflectivity series, statistical deconvolution allows the calculation of an autocorrelogram and prediction of the amplitude spectrum of the unknown source wavelet from the recorded seismogram. I applied multi-channel predictive deconvolution for the shot at location 43644 m with decon "gap" in the autocorrelogram of 7 time samples (7 ms), with a total 140 point filter length. Figure 2.8 shows the average autocorrelation function of the shot before and after predictive deconvolution. The reverberations of multiples and source bubble pulses (circled in the figures) disappear after predictive deconvolution. The power spectrum before and after applying predictive deconvolution is shown in Figure 2.7. The reverberations also disappear in the power spectrum after deconvolution.

Geometric spreading is defined as the decay of amplitude resulting from the distance traveled by the spherical wavefront. There are several techniques that compensate or correct the amplitude. A t-power scaling factor (t is the total traveltime from the source) is a commonly used technique which is independent of velocity. Each time sample in the trace is multiplied by a gain function as described by:

$$g(t) = t^{\alpha} \tag{2.1}$$

where t is time and α is some constant, commonly assumed to be 2 (Claerbout, 1985). The application of this formula is demonstrated in Figure 2.9 where the amplitude in the late time arrival is enhanced. Data are also bandpass filtered to remove noise outside the spectrum of the data.

The second major process, CMP stacking or summing all traces, is aided by regrouping the data into common midpoint (CMP) domain. Each subsurface reflection point is recorded from different source-receiver offsets on the surface. This allows one to apply velocity analysis, apply normal moveout (NMO) correction, and sum the data across all offsets of the CMP record. For horizontal layers, with no latteral velocity change, the reflection time recorded from the same reflection point increases with offset as per the hyperbolic equation (Yilmaz, 2001):

$$t^2 = t_0^2 + \frac{x^2}{v^2} \tag{2.2}$$

where t is two-way traveltime, x is source-receiver offset, v is stacking velocity, and t_0 is two-way vertical traveltime. Time samples for traces are corrected by shifting the sample record at this time to a corrected time of zero-offset (NMO correction). The data are then summed along the offset axis by simple summation or coherency stacking. This process increases signal to noise ratio and is designed to attenuate

coherent multiple energy. NMO corrections tend to stretch shallow events and thus the distorted part of the record is commonly "muted" by substituation of null values.

Stacking velocity analysis is a crucial processing step required for NMO correction and stacking. I chose to estimate velocities for CMPs at every 100th CMP location (625 m) using an automatic velocity picking tool (Fomel, 2009a) with muting assistance from visually-picked velocities. The visually-picked velocity projects the trend of the velocity to constrain the automatic picking as shown in Figure 2.10. The stacking velocity for the seismic line 12 is shown in Figure 2.11. Note the constant velocity of 1500 m/s above the water bottom.

In the case of dipping events, reflection points are not the midpoints and hence NMO is not sufficient to move data to their zero-offset reflection time. Dip-moutout (DMO) is another process that transforms the data from CMP to Common reflection point (CRP). The NMO equation is modified to account for the dip and becomes (Yilmaz, 2001):

$$t^2 = t_0^2 + \frac{x^2 cos^2\theta}{v^2} \tag{2.3}$$

where θ is the dip of the reflector in the vertical plane of the profile. DMO was a research focus topic 30 years ago. There were arguably difficulties in its implementation and whether it can be successfully applied. Generally, DMO can be applied in the cases where NMO processing can be applied (Hale, 1991). Nevertheless, DMO correction is especially important for poststack data diffraction imaging. The details are discussed in Chapter 4. Figure 2.12 shows the DMO stacked section of Line 12 of the Canterbury Basin. The DMO corrected stacked section reveals a slightly dipping sea floor. In addition, mounded reflections appear under the gently dipping sea floor between the shelf edge and slope toe suggesting the presence of large, mounded

aggraditional sediment drifts.

Migration, the third major processing step, collapses diffractions and moves structurally dipping events to their correct subsurface positions, thus increasing both latteral resolution and correct positioning of reflectors. Migration could be applied before stacking as prestack migration, or after stacking as poststack migration. Thus stacking is postponed in the case of prestack migration, and in this case, we stack image gathers instead of CMP gathers. Significantly, prestack migration negates the need for DMO corrections. Chapter 5 provides more details about the migration process.

Discussion

I applied the above processing steps to the Canterbury dataset Line 12. The steps include bandpass filter, amplitude correction, CMP sorting, velocity analysis, NMO correction, and DMO stacking. Although discussed as a general tool, deconvolution was not applied to the data because the multiple prediction algorithm discussed in Chapter 3 assumes that the source wavelet is present in the data. The DMO stack is generated after multiple attenuation and is used as input for processing workflows discussed in Chapters 4 and 5 which address diffraction separation and migration, respectively.

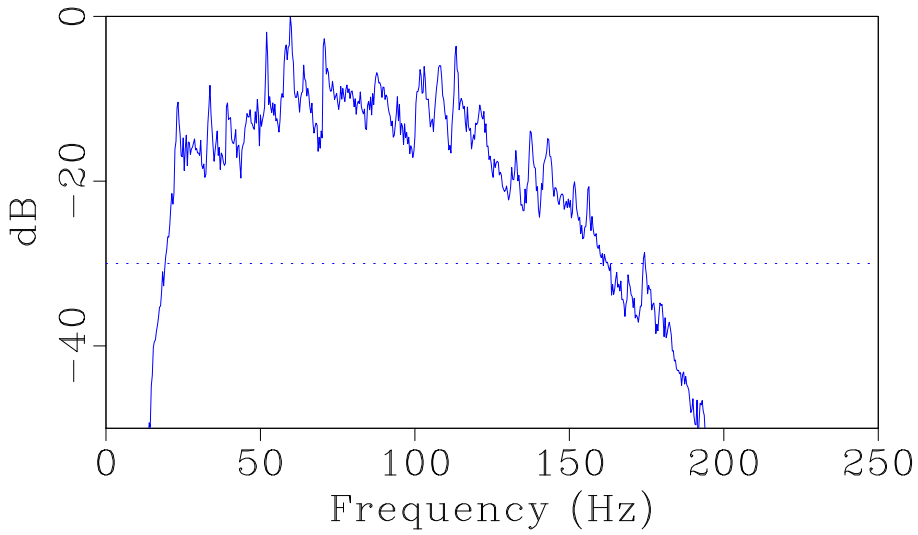

(a)

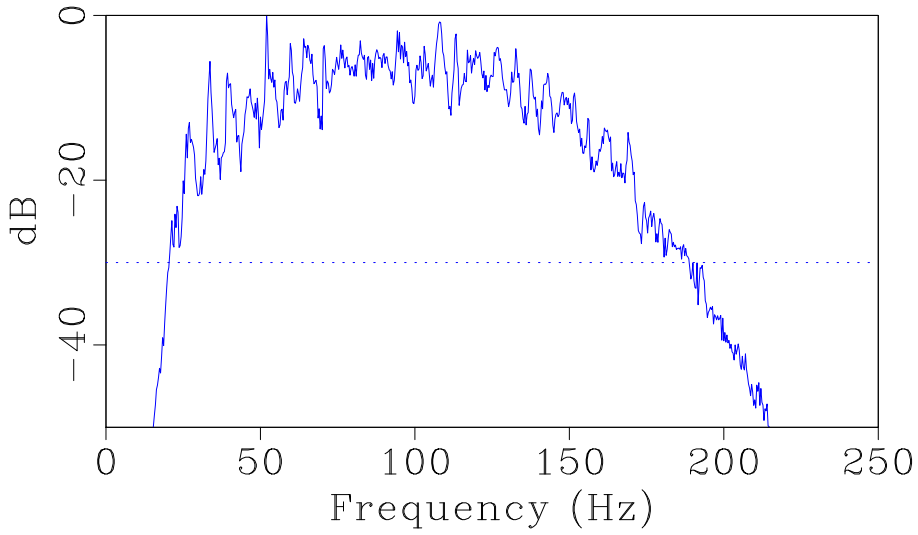

(b)

Figure 2.7: Power spectrum before predictive deconvolution (a). Power spectrum after predictive deconvolution (b). The spectrum was computed for a shot at location 43644 m in the profile. A multi-channel predictive deconvolution with "gap" of 7 time samples (7 ms) and 140 point filter length (140 ms). Note the improved spectrum energy from 100-150 Hz for the "gap" decon.

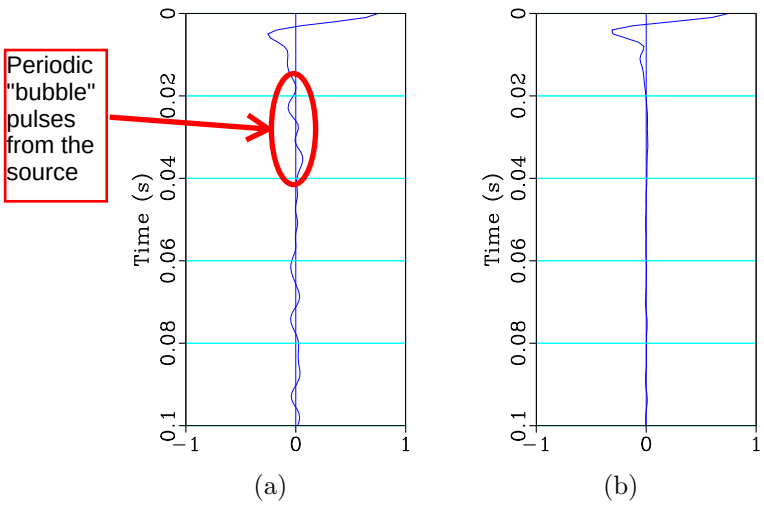

Figure 2.8: Autocorrelation for the same shot in Figure 2.7 (shot at location 43644 m in the profile). Before applying decon (a). After applying decon (b). Notice that the airgun bubble pulses are attenuated after predictive deconvolution

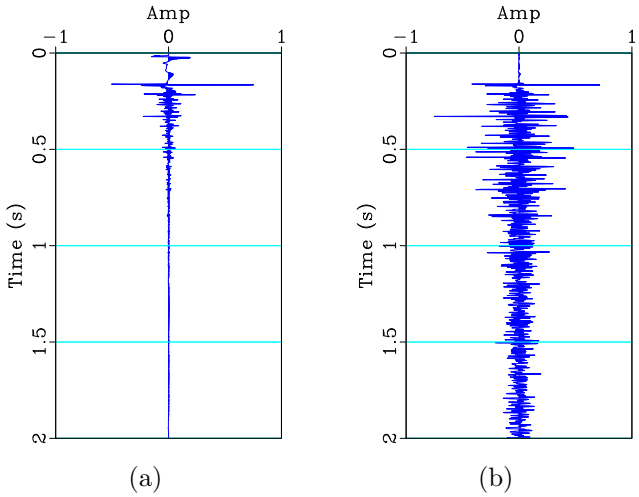

Figure 2.9: Amplitude of one trace (a) from the shot in Figure 2.7 before applying time variant scaling to improve late arriving amplitudes. After applying the time varying scaling (b).

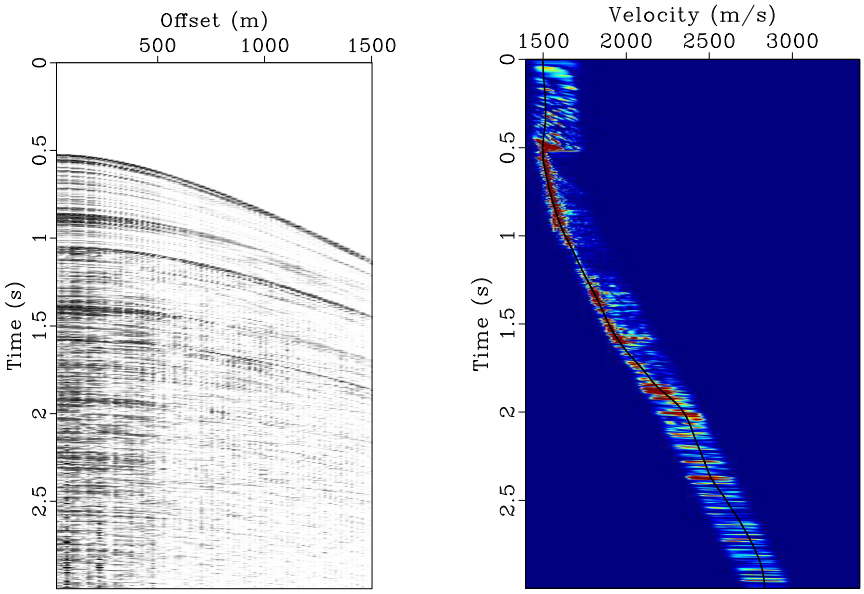

(a)

(b)

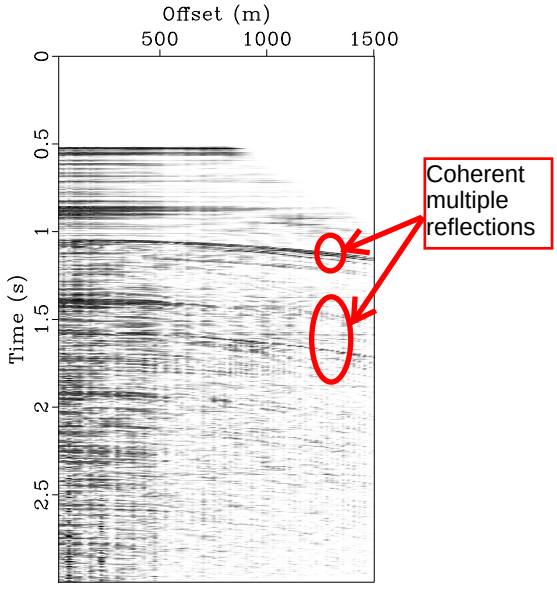

(c)

Figure 2.10: CMP at location 3218 m (a). Semblance scan of NMO velocity estimates, with mute around visually picked velocities (b). NMO correction is applied using the picked velocity (c). "Under-corrected" curved events after NMO correspond to multiple reflections.

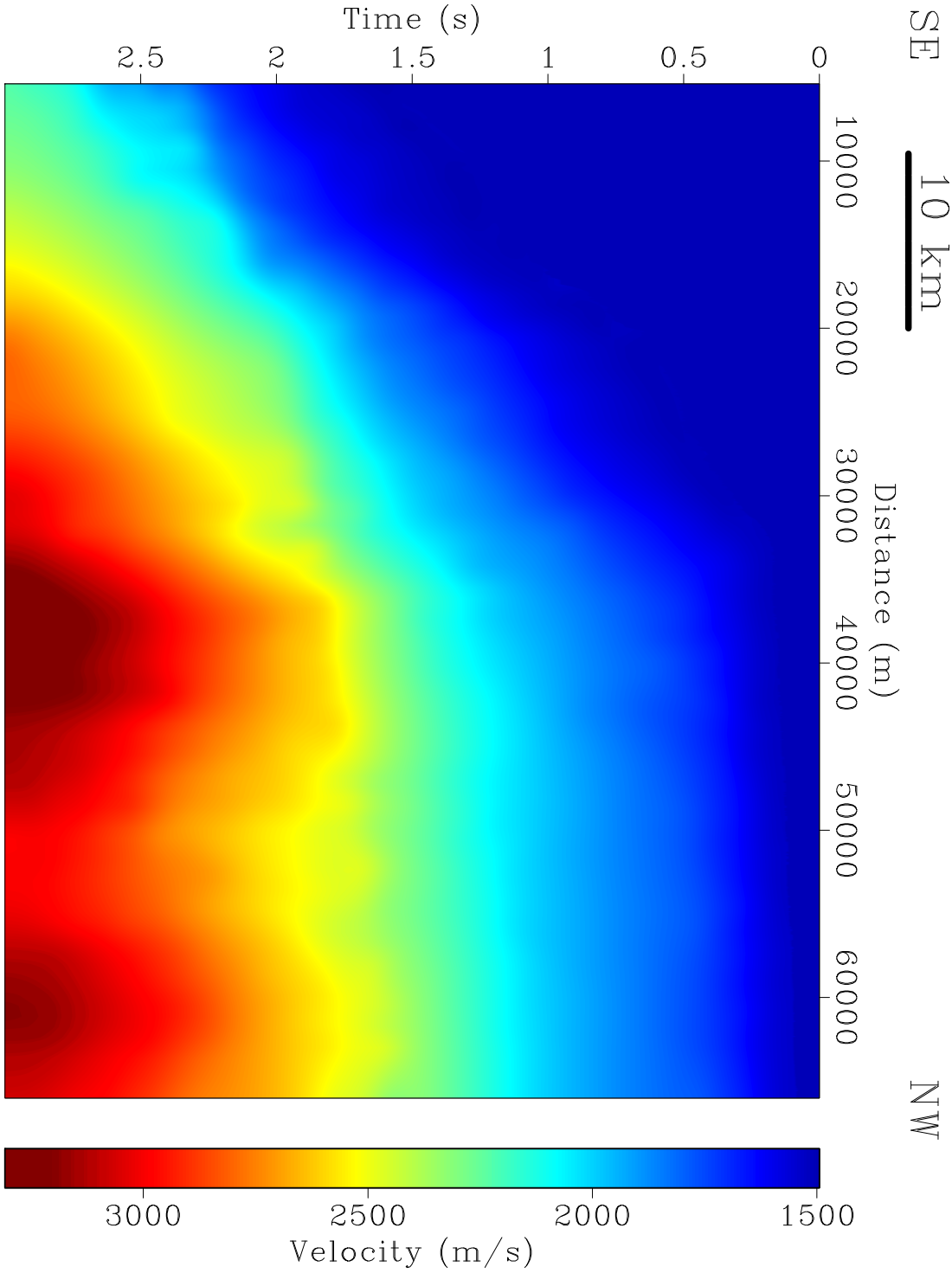

Figure 2.11: NMO velocity profile for Line 12 extracted using automatic velocity picking tool, aided with mute using visually picked velocity

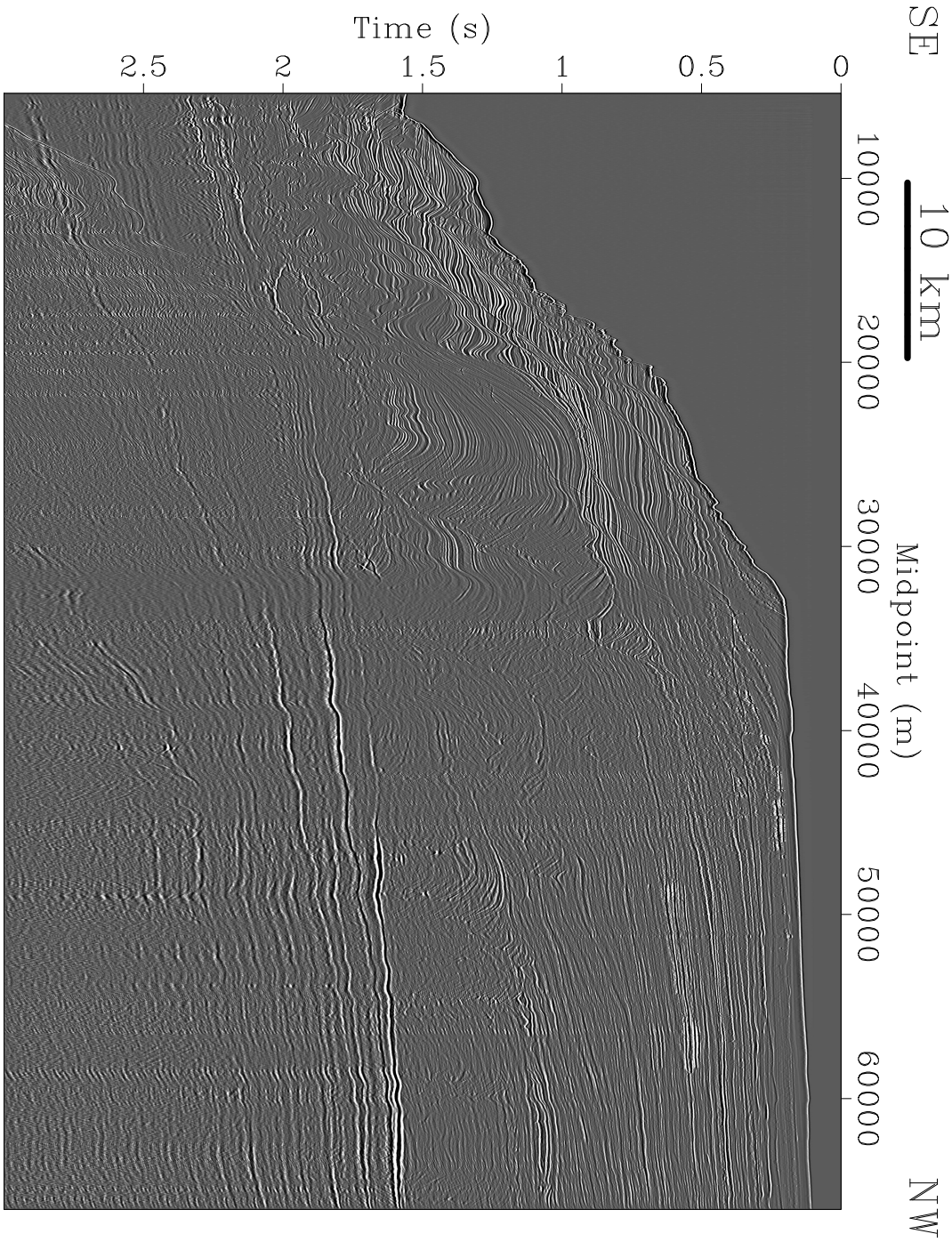

Figure 2.12: DMO stacked section of profile 12 of the Canterbury Basin, New Zealand. Note the slightly dipping sea floor and the mounded reflections to the left of the figure which appear under the gently dipping sea floor between the shelf edge and slope toe suggesting the presence of large, mounded aggraditional sediment drifts

Chapter 3

Surface-related multiple attenuation

Introduction

Multiple reflected energy is defined as seismic energy that has been reflected more than once (Sheriff, 2002). Multiple energy is a kind of coherent noise correlated from one trace to another in seismic records, and thus not removed by conventional bandpass filters. Although multiple events in seismic data potentially carry information about the earth subsurface, they often obstruct the primary signal which represents primary reflections coming from reflectors in the subsurface. Moreover, if multiples are not removed, they may be misinterpreted as primaries (Weglein, 1999). There are two general types of multiples: short-period multiples and long-period multiples. Short-period multiples (sometimes from the sea floor) arrive so soon after the primary signal that they add a tail to the primary signal and obstruct stratigraphic details (Sheriff, 2002). In some cases, short-period multiples can be attenuated by source-wavelet deconvolution (Yilmaz, 2001). On the other hand, long-period multiples arrive as distinct events due to the additional time they travel downward before reflecting back and being recorded at the surface (Sheriff, 2002).

The long-period multiples may be attenuated using several different methods which can be classified into two broad categories. There are methods that exploit distinguishing properties or features between multiples and primaries, and methods that are based on prediction of multiples and subsequent subtraction (Weglein, 1999).

The first category is typically based on time-series methods and apparent stacking velocity. Table 3.1 lists common methods of the first category which can be grouped into multiple attenuation based on periodicity of the reflection and separability in the $t-x$. For example, transforming shot gathers from $t-x$ domain into the $\tau-p$ domain using slant stack, where p is the inverse of horizontal phase velocity, maps hyperbolic events into ellipses and separates the overlap of multiples in $t-x$ domain. Multiples have the same p value of the parent primary but delayed in time, and hence appear periodic in the $\tau-p$ domain, where they are not necessarily periodic in the $t-x$ domain. Thus, predictive deconvolution can be used to attenuate multiples in the $\tau-p$ domain (Stoffa, 1989).

Multiples can also be distinguished from primaries based on separability features in the $t-x$ domain. For example, CMP stacking attenuates improperly NMO corrected multiples compared to the properly NMO corrected primaries. Another example, after NMO-correction using the correct velocity model, CMPs are transformed from $t-x$ domain into $\tau-p$ domain using a parabolic Radon-transform (RT) method (Hampson, 1986; Foster and Mosher, 1990). In this Radon domain, primaries and multiples are focused in different regions of the $\tau-p$ space due to the difference in their moveout. Thus, exploiting the separability feature allows for muting/filtering of the multiples. This method has also been applied for multiple attenuation in the image space, migrated data (Sava and Guitton, 2005). Instead of working with CMPs, one could apply RT to image gathers. In the image-gather domain, primary events are assumed to be flat while the multiples are curved. Although the Radon-transform is robust and commonly used multiple attenuation method (Foster and Mosher, 1990), it is not necessarily the optimal method for complex wavefield propagation in which the travel time is not hyperbolic; or shallow depth water in which the difference in

moveout between primaries and multiples is not large enough (Bishop et al., 2001).

The second category, prediction and subtraction, is based on prediction from modeling or inversion of seismic records. Table 3.2 lists three different prediction and subtraction methods: wavefield extrapolation, feedback loop, and inverse scattering. There are different requirements for each method. For example, feedback loop is an inversion method that uses a velocity model to attenuate all kinds of multiples. However, this method does not require the velocity model or knowledge of subsurface geology to attenuate surface related multiples which in this context is referred to as surface related multiple eliminations or SRME (Verschuur et al., 1992; Dragoset and Jeričević, 1998). Surface multiples are the ones that have at least one downward reflection at the sea surface in their ray path.

I choose to attenuate the multiples in the Canterbury dataset of Line 12 using surface related multiple prediction-and-subtraction method for two reasons. Surface multiples appear strong in seismic records because of the strong reflection coefficient at the water surface (Dragoset and Jeričević, 1998). Therefore, the effect of surface related multiples on seismic records is more pronounced than internal multiples. In addition, other multiple attenuation methods, such as RT, are potentially biased towards reflection data and during demultiple attenuation step, diffractions may also be destroyed. I predict the surface related multiples using an algorithm proposed by Dragoset and Jeričević (1998). Then, I subtract the predicted multiples adaptively, as proposed by Fomel (2009a).

Domain	**Algorithm**	**Feature**
t	predictive decon	periodicity
$\tau - p$	Radon transform + predictive decon	periodicity
$t - x$	stacking	separability
principal comp.	eigenimages + reject filter	separability
$f - k$	2-D FT + reject filter	separability
$\tau - p$	Radon transform + reject filter	separability
$f - k$	3-D FT + reject filter	separability

Table 3.1: Multiple attenuation based on properties that differentiate primaries from multiples. Table from Weglein (1999)

	Modeling and subtraction	**Inversion**	**Inversion**
	Wavefield extrapolation	Feedback	Inverse-scattering Series
Types of multiples	Water-bottom, peg-leg and first-layer reverberations	Free surface multiples, Internal multiples (all order one interface at a time)	Free surface multiples, Internal multiples (all order one interface at a time)
Fundamental physical unit	Water-layer and ocean-bottom	Free-surface + Interface(reflector)	Free-surface + Point scatterer
Additional information needed	water-depth(a priori) Adaptive subtraction (a posteriori)	None for free-surface Internal: A priori velocity model implicit for CFP operator; and updating; or an a posteriori interpretative decision at each reflector	None for free-surface or internal multiples

Table 3.2: Multiple attenuation based on prediction and subtraction. Table from Weglein (1999)

Surface-related Multiple Prediction

The multiple reflected events that appear in seismic data can be divided into two classes based on where the downward reflections in their raypaths occur: internal multiples and surface predictable multiples. Internal multiples have their downward reflections initiated at the water bottom or below (Figure 3.1(d)). Surface-predictable multiples, on the other hand, are events that have at least one downward reflection initiated at the water surface (Figures 3.1 (a),(b), and (c)). Thus a surface-predictable multiple, no matter how complicated its raypath, consists of segments that, from the surface perspective, may be considered primary events. Intuitively, surface multiple attenuation is the task of using primary events to predict multiple events from surface reflection locations.

The surface multiple attenuation algorithm, described here, is a prestack technique of using of a surface-recorded 2D wavefield that aims at removing all orders of all surface multiples present within the wavefield. The algorithm requires no assumptions or modeling regarding the positions and subsurface reflection coefficients of the multiple-causing reflectors. The algorithm attempts to attenuate not only reflected multiples but also refracted multiples and converted-wave multiples. The algorithm formulates the surface multiple prediction problem in a from similar to the diffraction-aperture problem of classical optics (Dragoset and Jeričević, 1998).

To intuitively describe the algorithm, I use Figure 3.2(a). The figure shows a survey configuration where shooting goes from right to left. S denotes the source location, R denotes the receiver location, and A is the downward reflection point of a multiple at the sea surface. The question mark shows that the behavior of the raypath is unknown in the subsurface. The multiple appears in shot S and receiver R, which

can be decomposed into two primaries SA and AR. Thus, if we identify the two primary segments, convolve them and multiple by -1, to account for the sea surface reflection coefficient, we can predict the multiple. However, there is a challenge in estimating the amplitude of the predicted multiple because simple convolution does not account for wave propagation in 3D. Another challenge is to locate point A.

To address these two challenges, we can use the image point concept (Sheriff, 2002). We replace the reflected ray at the surface with one that passes through the surface and straighten the lines that connect S,A, and R as shown in Figure 3.2(b). Then, we treat the event as wavefield as shown in Figure 3.2(c). On the left, the surface is illuminated by primary wavefield $PS(x,t)$, which will appear in the common shot record for source position S, on the right, primary $PR(x,t)$ is a wavefield that will appear in the common receiver record for receiver position R, and the variable x represents position along the in-line direction. The problem is defined as: given a wave source at position S, measure the disturbance on the other side of the aperture at position R.

The Kirchhoff integral, a mathematical statement of Huygens's principle, provides a way to solve the diffraction aperture problem and hence also provides a solution to the surface multiple prediction problem (Dragoset and Jeričević, 1998). The task is to calculate the illumination from S that is incident on the aperture and the illumination at R arising from placing a secondary source positioned anywhere within the aperture. However, in this formulation, the limited recording aperture of the measured wavefields, because of the finite extent of the marine cable, makes the surface multiple prediction imperfect. The mathematical form of the Kirchhoff integral is

described by:

$$\begin{aligned} m(S,R,t) = & -t^{-1/2}F_{\omega\to t} \\ & \left\{(1-i)\sqrt{\frac{\omega}{4\pi}}\int_A dx F_{t\to\omega}[\sqrt{t}P_S(x,t)]F_{k\to x}\right. \\ & \left.\left\{\sqrt{1-\left(\frac{kV}{\omega}\right)^2}F_{x\to k}F_{t\to\omega}[\sqrt{t}P_R(x,t)]\right\}\right\} \end{aligned} \tag{3.1}$$

where i is the square root of -1, F is Fourier transform, V is the speed of sound (propagation velocity) in water, k is x component of the wavenumber, $\omega = 2\pi f$, and A is the surface aperture, or cable length. This equation basically says that for each x in the aperture, we need to convolve corresponding traces from PS and PR, stack, and multiple by -1. Thus the prediction of a surface multiple can be formulated as

$$M_1 = PO_kP \tag{3.2}$$

where O_k is the Kirchhoff operator, M_1 is the first order multiple, and P is the primary. However, this equation predicts only the first order of multiples and assumes that the primary events are known. The equation can be modified as

$$M_i = PO_kM_{i-1}, \tag{3.3}$$

where M_i is i_{th} order multiple. In this equation, M_0 corresponds to primary P, and i order multiple can be computed from $i-1$ order multiple. This allows breaking the data D into primaries and all orders of multiples

$$D = P + M_1 + M_2 + ... + M_n \tag{3.4}$$

Using equations 3.3 and 3.4, we arrive at the following equation

$$D = P(1 + O_kD_{tr}), \tag{3.5}$$

where $D_{tr} = D - M_n$. And if the $(1 + O_k D_{tr})$ has an inverse $(1 + O_k D_{tr})^{-1}$, then we get

$$P = D(1 + O_k D_{tr})^{-1} \tag{3.6}$$

This equation says that, we may get the primary wavefield P directly from the recorded wavefield D. To account for the duplication of source-wavelet w resulting from the convolution process, equation 3.3 is modified and becomes

$$M_i = w^{-1} * P O_k M_{i-1} \tag{3.7}$$

where w^{-1} is the inverse of source-wavelet. Thus equation 3.6 is modified and becomes (Dragoset and Jeričević, 1998)

$$P = D(1 + w^{-1} * O_k D_{tr})^{-1} \tag{3.8}$$

In the $f - x$ domain, we use an approximated fixed wavelet to compute an estimate of the surface multiple wavefield for each frequency component in the data set using 3.4, and 3.7, and in the matrix formulation, the O_k is replaced by matrix multiplication, we reach to equation

$$M = D - P = D - D(1 - w^{-1} D_{tr})^{-1} \tag{3.9}$$

where w^{-1} can vary with frequency only. Then to transform the predicted multiples from frequency domain into the time domain we apply the equation

$$m(S, R, t) = t^{-1/2} F_{\omega \to t}[m(S, R, \omega)] \tag{3.10}$$

The predicted multiples are now ready for adaptive subtraction.

It is important to note that the algorithm is affected by imperfections in the input dataset and is based on several assumptions including:

1. If a dataset contains a particular surface multiple, then it must also contain all of the primary pieces that make up that multiple. Likewise, if a dataset contains certain primary events, then it must also contain all of the surface multiples that can be built from those primary events.

2. The dataset must be free of any distortions that might affect some events differently than others, since the prediction is done by combining different events. Dragoset and Jeričević (1998) discuss in details the requirements and assumptions that, if not met, may lead to less effective surface-multiple predictions.

Adaptive Multiple Subtraction

In general, the predicted multiples using the algorithm explained above differ from the real multiples present in the dataset. The difference occurs in both amplitudes and phases. One reason for that comes from the convolutional process which does not account for 3D geometric spreading of energy. As a result, direct subtraction of the predicted multiples from the dataset may not give useful results. Therefore, in practice, matched filtering is used to account for the differences in amplitude and phase of the predicted multiples (Verschuur et al., 1992; Dragoset and Jeričević, 1998). An optimal approach to matched filtering is to apply a nonstationary adaptive filtering method Margrave (1998). The nonstationary adaptive filtering is a nonstationary regression problem that can be used to enhance the predicted multiples. Fomel (2009a) extends the idea of nonstationary regression to regularized nonstationary regression and shows that the extension yields plausible results. Moreover, this extension eliminates the need for breaking the dataset into small subsets of the data.

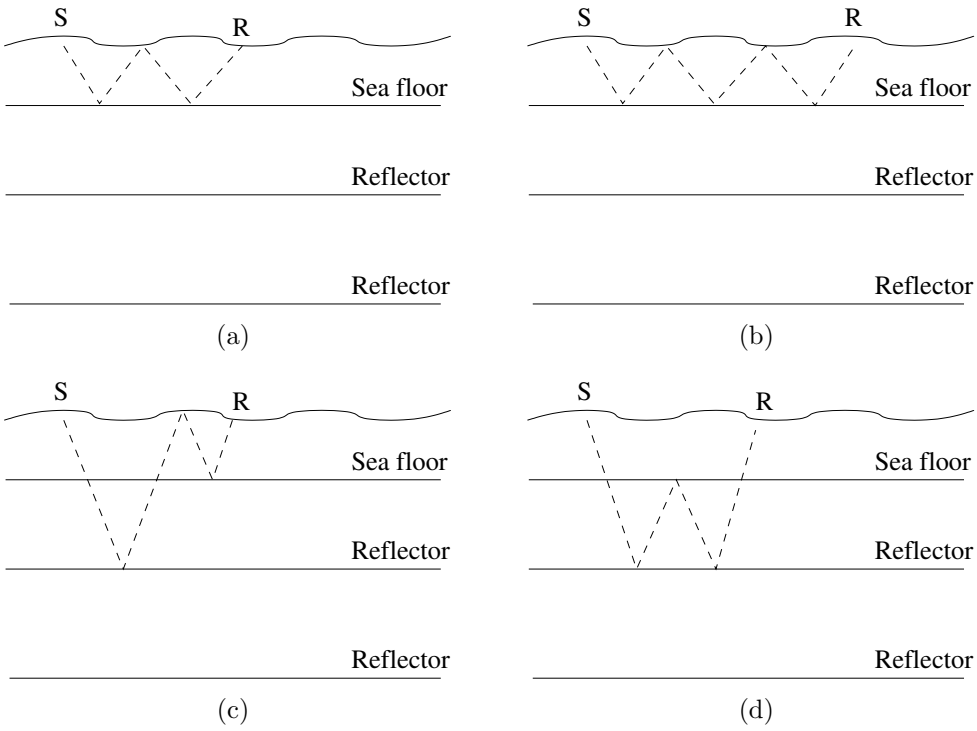

Figure 3.1: Raypaths for some common multiple reflection events: water-bottom first-order surface multiple (total 3 reflections)(a), water-bottom second-order surface multiple (total 5 reflections)(b), peg-leg first-order surface multiple (total 3 reflections) (c), internal multiple (d). Notice that Figures (a),(b), and (c) have a downward reflection in their ray path at the sea surface while Figure (d) does not. A synthetic CMP model for multiples in the figures will be used to illustrate the surface multiple prediction and adaptive subtraction later in the chapter.

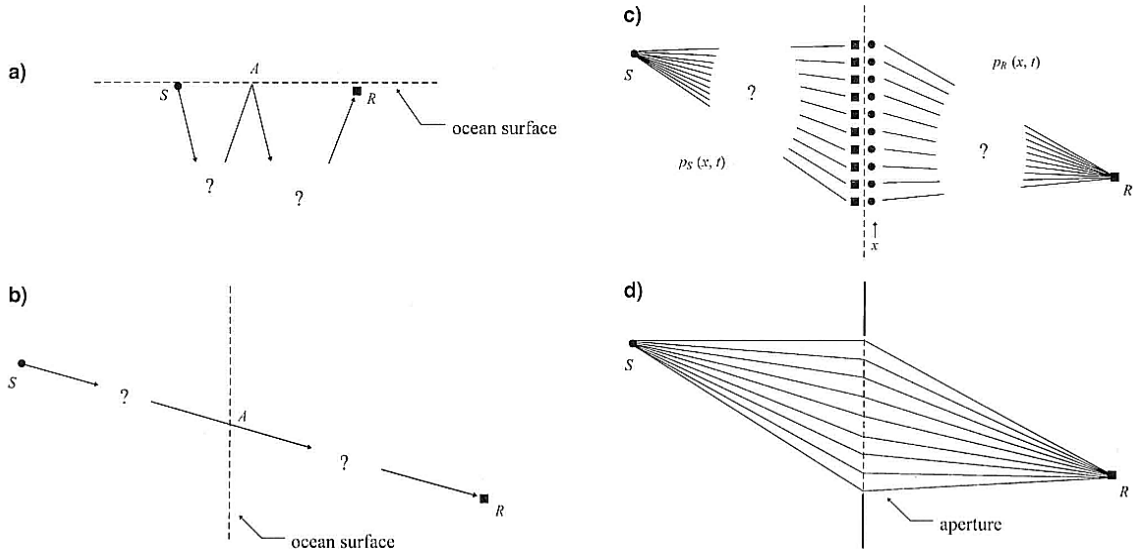

Figure 3.2: S is a source, A is downward reflection point, R is a receiver (a). The multiple SAR may be considered as two primaries SA and AR. The question mark indicates that the behavior of the multiples in the subsurface is not known. Using the image concept (b) by assuming rays pass through the sea surface and straightening the rays. Replacing the rays with wavefields (c). The problem of surface multiple prediction resembles the diffraction aperture problem (d). Figure from Dragoset and Jeričević (1998).

Nonstationary regression

Consider a "master" signal $m(\mathbf{x})$, where $\mathbf{x}$ represents the coordinates of a multidimensional space, and a collection of slave "signals" $s_k(\mathbf{x})$, $k = 1, 2, \ldots, N$, where these slave signal are translates of the master signal. The regression problem corresponds to the problem of match filtering between $s(\mathbf{x})$ and $m(\mathbf{x})$. It is a convolution with an unknown matching filter. The nonstationary regression allows its coefficients b_k to change with $\mathbf{x}$. The error becomes

$$e(\mathbf{x}) = m(\mathbf{x}) - \sum_{k=1}^{N} b_k(\mathbf{x})\, s_k(\mathbf{x}) \ , \tag{3.11}$$

Minimization in a least square sense of the problem is ill-posed, because one can get more unknown variables than constraints. The remedy is to include additional constraints that limit the allowed variability of the estimated coefficients. Instead of using Tikhonov regularization to solve the equation, Fomel (2009a) suggests using shaping regularization (Fomel et al., 2007) to constraint the variability of the coefficients.

Synthetic Example

To illustrate multiple attenuation, I generated a synthetic CMP gather, and predicted the surface multiples by transforming the data into $f - k$ domain and multiplying the data with itself and by -1 (Figure 3.3). On the right is a CMP gather with 3 primary events (first, second, and fourth). On the left of the figure is the predicted surface multiples only. Offset axis on the multiple side was reversed so it is easy to visually relate the multiples with the ones in the CMP gather. The figure also shows that the internal multiple (fifth event) was not predicted.

I ran the regularized nonstationary regression using an algorithm that takes both the synthetic CMP and the predicted multiples and produces the estimated multiples. The estimated multiples have the phase and amplitude corrected so the multiples better match the real multiples present in the CMP gather. Figure 3.4(b) shows the estimated multiples resulting from running the algorithm. The estimated multiples have better continuity at near offsets and one could also notice that both the primary, fifth event, and the internal multiple were not affected. Figure 3.4(d) shows the CMP gather after attenuating the multiples. For this simple experiment, the multiple attenuation performed well. The three multiple events (3,6,and 7) were attenuated successfully without affecting other events including the internal multiple (event 5).

Figure 3.5(a) shows a little variations of the filter coefficients for zero-lag coefficients. However, there is a noticble increase in variations at zero-offset for each of the three multiple events (circled in the figure). The variation is expected due to the difference in the amplitude of the predicted multiples (Figure 3.4(a)) and the real multiples (Figure 3.4(c)) at zero-offset. The amplitudes of the predicted multiples at zero-offset appear week. Thus the adaptive subtraction attempts to adjust the amplitudes at zero-offset of the predicted multiples for more effective subtractions. Figure 3.5(b) shows the variations of the mean of the filter coefficients which gives an indication of the varaibility of the coefficients. One may use these figures to observe and control the amount of variability of the filter coefficients. These also give an indication of the amount of data to be used for adaptive subtractions and, gives a control over the estimation process. Too much variablity in the filter coefficients may results in subtracting primaries.

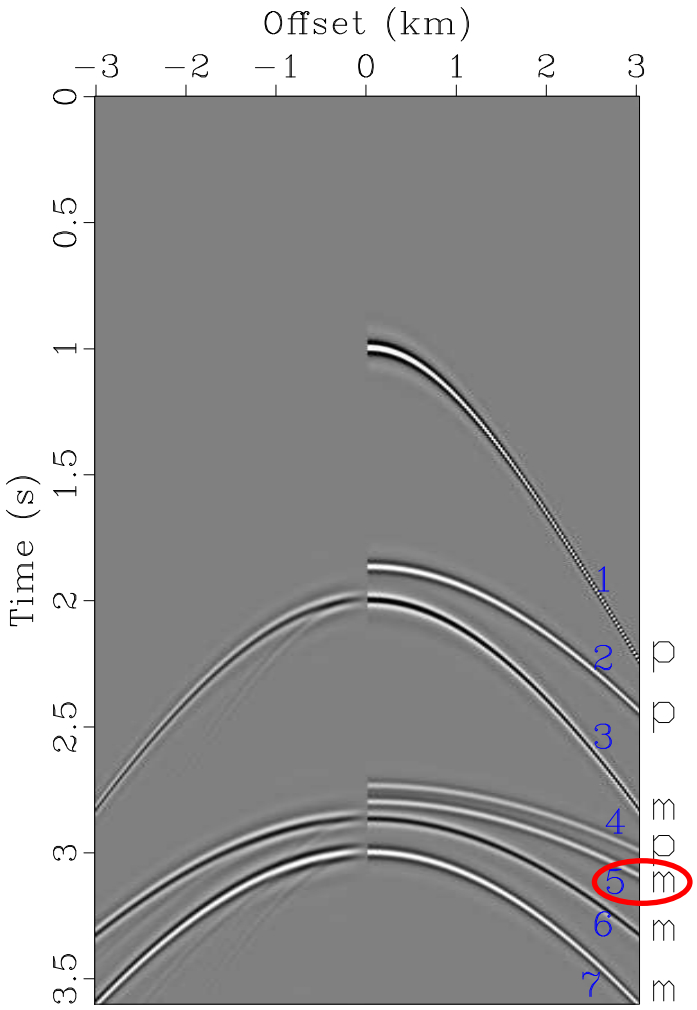

Figure 3.3: Synthetic CMP gather, right, with three primaries (first event, second event, and fifth event). Predicted multiples, left, generated by taking the CMP gather from t-x domain to f-k domain and multiplying the data by itself and by -1. The offset axis of the predicted multiples was reversed to facilitate comparison. Notice that the internal multiple, fifth event (circled), was not predicted by the convolution process.

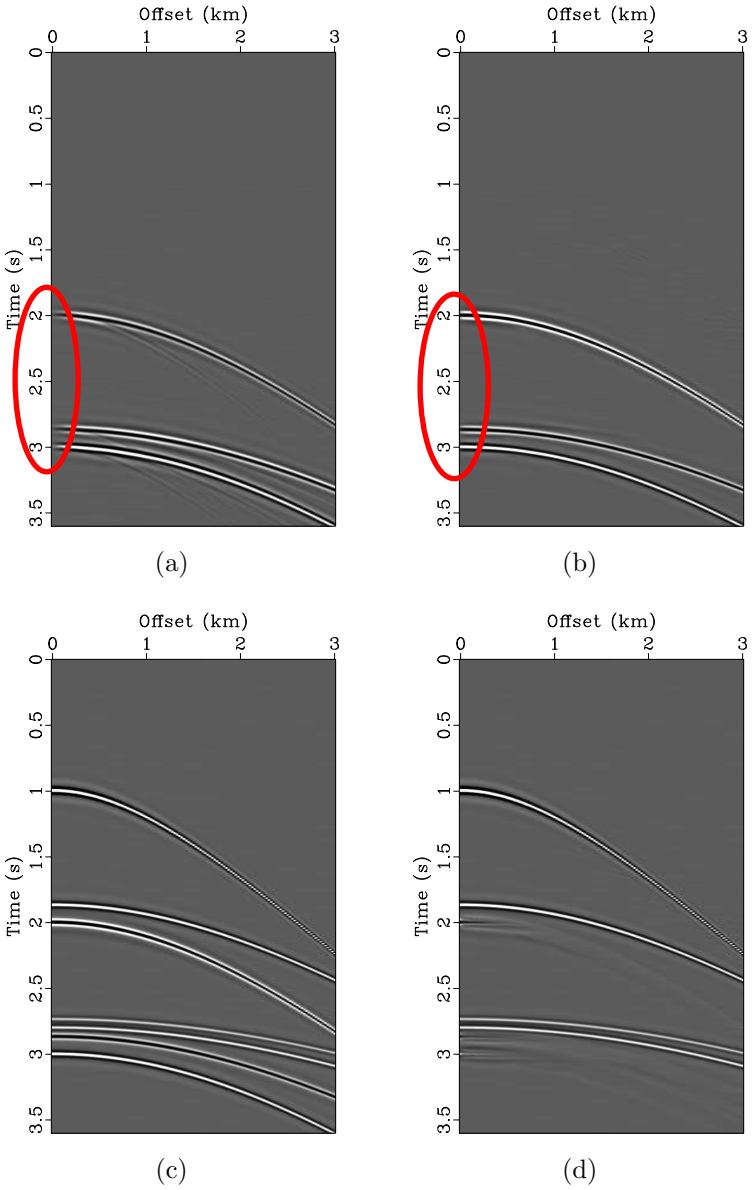

Figure 3.4: Predicted multiples (a) of the CMP gather in Figure 3.3. Estimated multiples using nonstationary regularized regression (b) by shaping regularization. The CMP gather before multiple subtraction (c). The CMP gather after multiple subtraction (d).

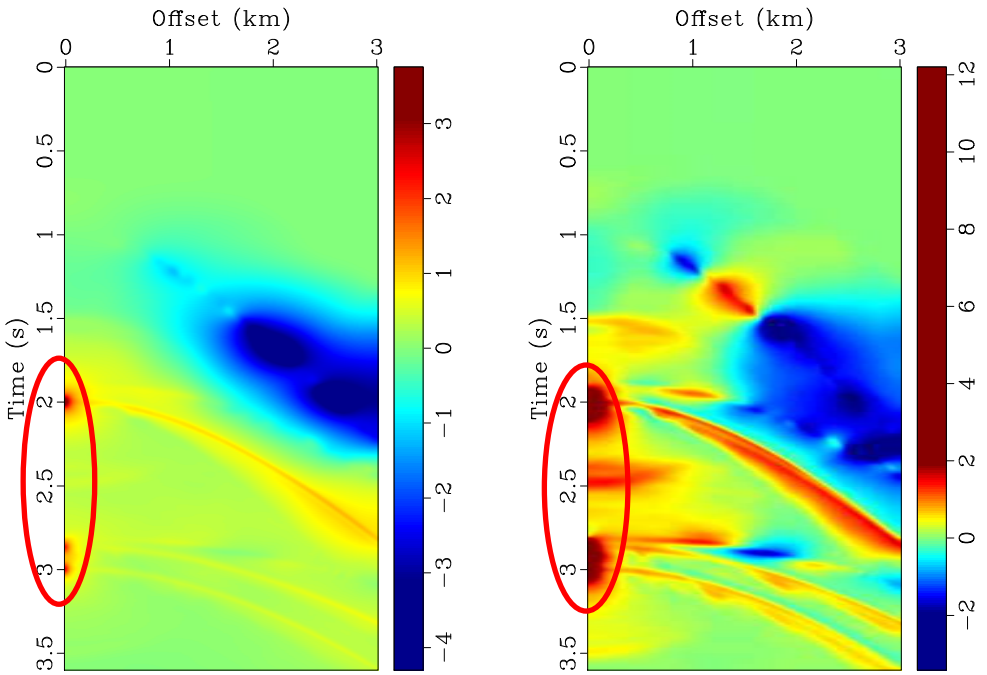

(a) (b)

Figure 3.5: Variation of filter coefficients for nonstationary shaping regularization regression applied using the predicted multiples and the data in 3.3. Zero-lag coefficients (a). Mean coefficients (b). Notice that at zero-offset the variation increases to account for the difference in amplitudes between the predicted multiple and real multiples.

Seismic Field Data

I applied the surface-multiple prediction algorithm to shot gathers from Line 12 from the Canterbury Basin dataset. The adaptive filtering process requires large computer memory. Therefore, I decomposed both the data and the predicted multiples into 120 common-offset gathers. Then, I applied the adaptive filtering algorithm, in parallel on each offset gather, using both the predicted multiples and the raw data. Figures 3.6 and 3.7 show the near-offset data from both raw shots and predicted multiples, respectively. The multiple energy in Figure 3.7 differ from the one in Figure 3.6. A clear difference in the amplitude appears in the left part of the figures (circled in the figures) while the right part shows noisy predicted multiples that are different from the actual recorded multiples.

The result of applying shaping and regularization match filtering using the near-offset data is shown in Figure 3.8. The estimated multiples are much closer to the real multiples which appears clearly in the left part of the figure (circled). Unlike the noisy predicted multiples, the estimated multiples are closer to the actual recorded multiples in the right part of the figure (circled). Figure 3.9(a) shows the variations of filter coefficients for zero-lag data. Similar to the idea in the synthic example earlier, the variations of filter coefficients are expected to take place in the areas where a difference in amplitudes and phases of multiples exists. Increased variations of the filter coefficients is noticeable in the left and right sides of the figure where the adaptive filtering attempts to correct for the less accurate predicted multiples. Figure 3.9(b) shows the mean variations of the filter coefficients for the adaptive match filtering.

Figure 3.10 shows a shallow water depth of the DMO stacked section before

and after surface-related multiple attenuation. The first order of water-bottom multiple (circled in the figure) disappears after multiple attenuation. The primary at midpoint 55000 m and around time .3 s, which overlays a multiple was partly affected. Figure 3.11 shows a good results of a peg-leg multiple attenuation (circled in the figures). The previous two figures demonstrate the capacity of the adaptive multiple attenuation applied of surface-related multiples to the Canterbury dataset. One drawback of the method may be observed for area where the sea floor is dipping. Figure 3.12 shows the results of the multiple attenuation applied on the stack section from the left part of the seismic line. The multiple energy (circled in the figure) was only reduced. This portion of the section included steep sea floor geology and thus greatly complicated the ability to predict multiples.

Discussion

Surface multiple prediction and adaptive subtraction using shaping and regularization is a good combination method for multiple attenuation. The surface related multiple prediction does not require velocity model, and only manipulates the recorded seismic data to predict the surface multiples which are stronger events than other types of multiples. The surface related multiple prediction algorithm, however, requires a dense and regularized acquisition geometry. For example, interpolating missing near offsets attempts to achieve regularized geometry. The predicted multiples may not be close enough to the real multiples and, therefore, one need to apply adaptive filtering to correct for phase and amplitude differences.

There are a number of extra steps I considered for the prediction step. I muted the direct arrival events to avoid false multiple prediction. In addition, the source-wavelet deconvolution was not applied since the source-wavelet is assumed

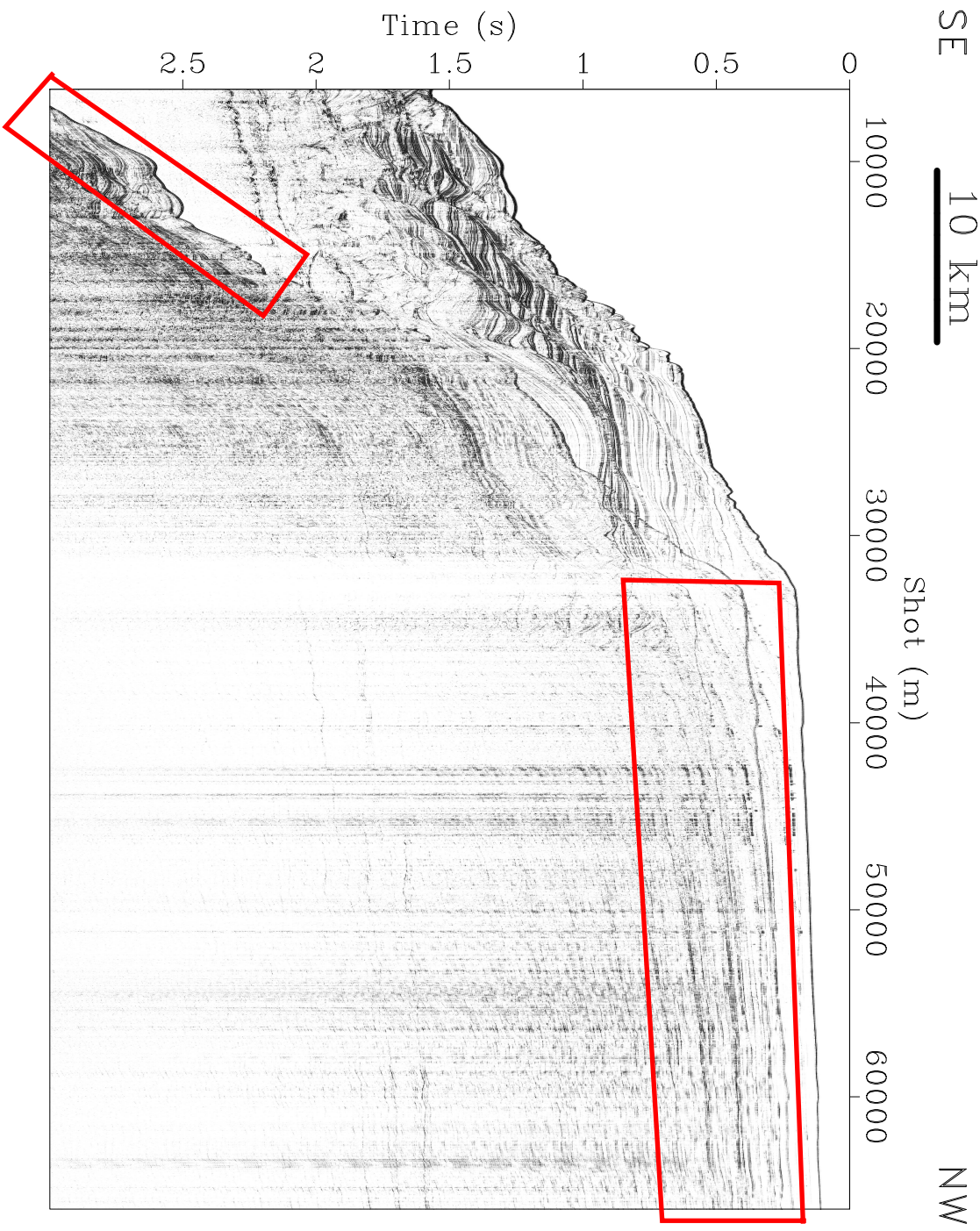

Figure 3.6: Near-offset data without multiple attenuation. The left part and shallow water depth (circled) show a dominent water-bottom multiple energy.

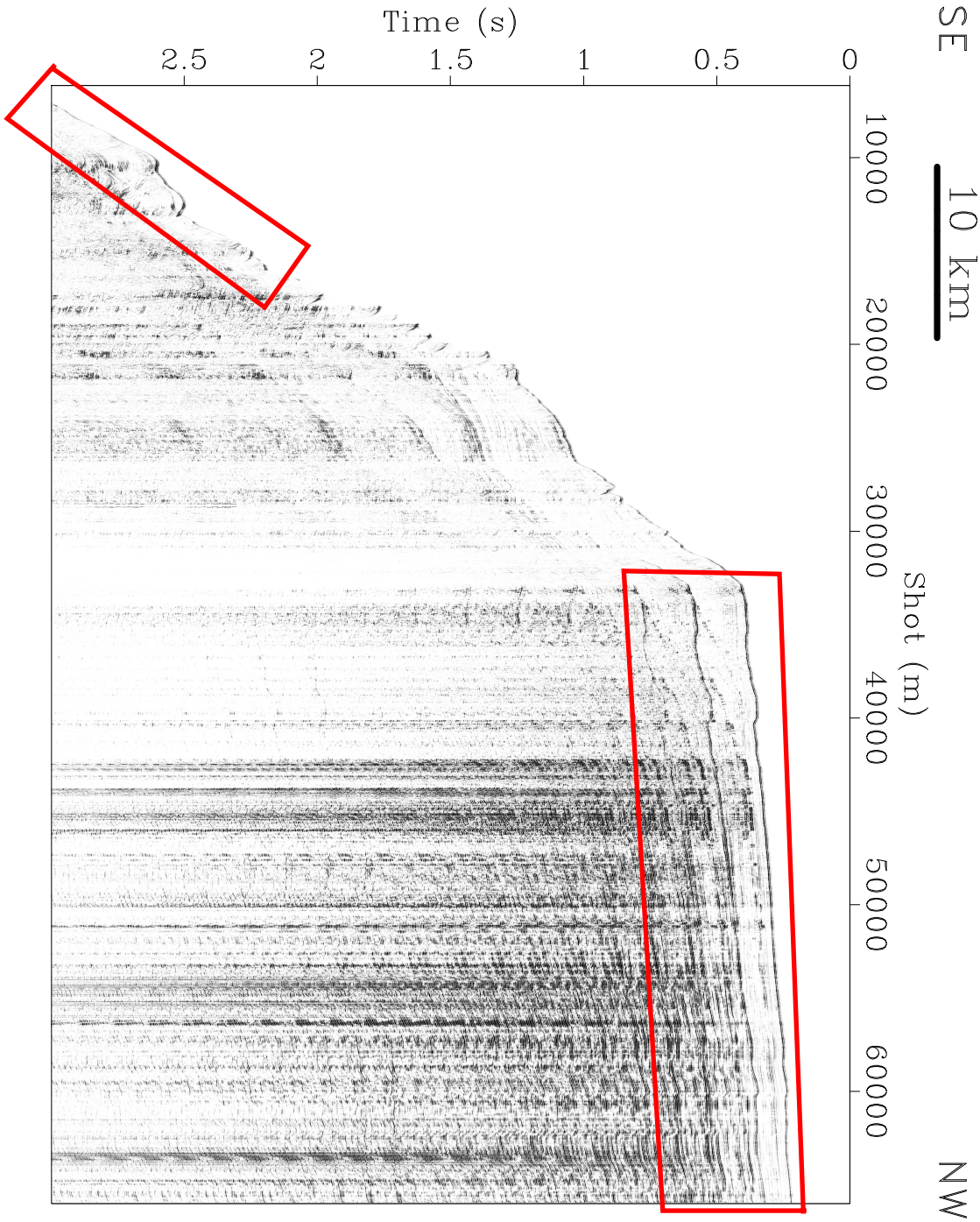

Figure 3.7: Predicted multiples after applying the surface multiple prediction algorithm to the near-offset data. The left part (circled) shows imperfect predicted multiples while the right part (circled) shows noisy predicted multiples. The predicte multiples requires refinement for proper subtractions.

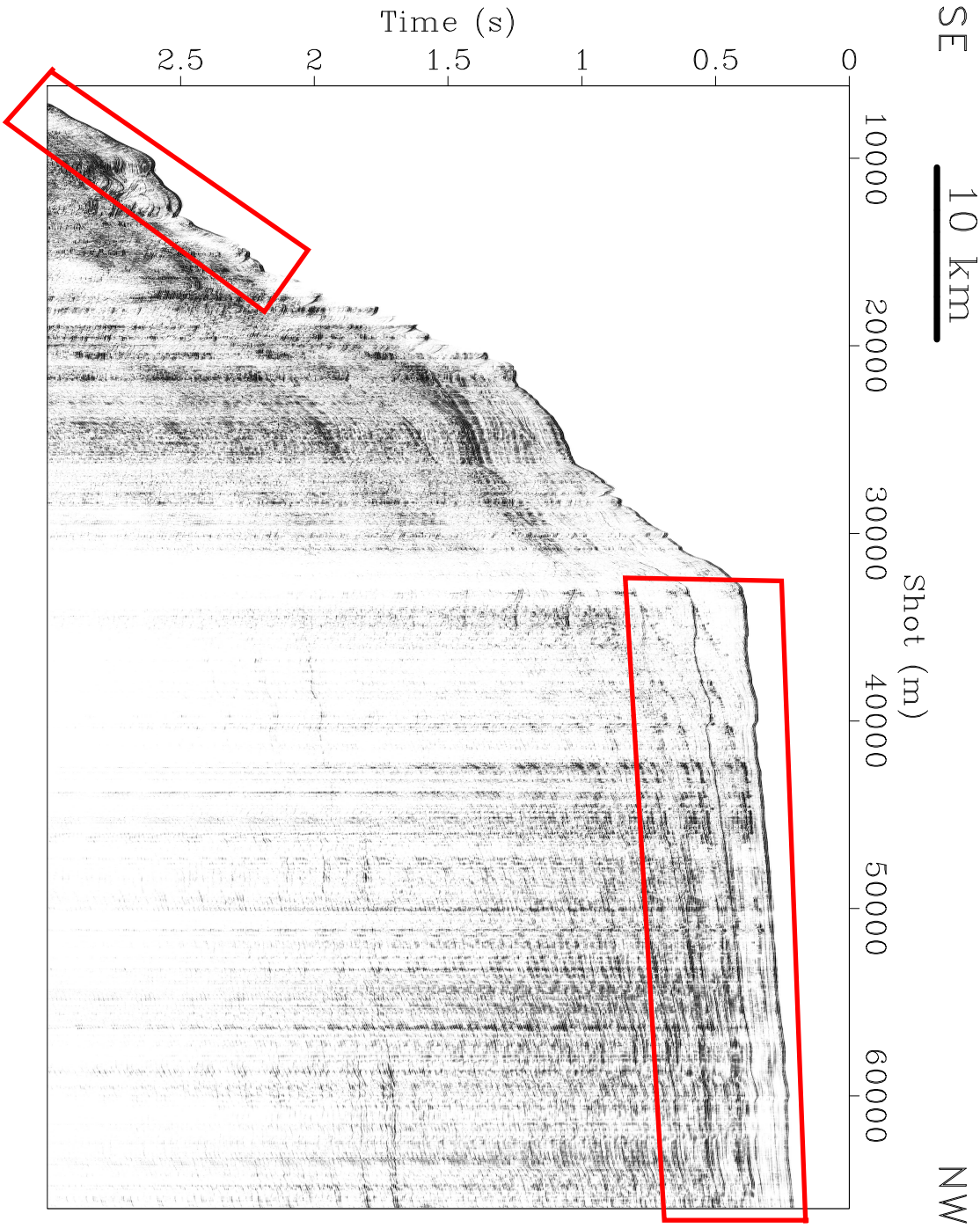

Figure 3.8: Estimated multiples obtained after applying shaping and regularization nonstationary regression method. The estimated multiples are better approximation to the real multiples. The enhancements to the prediction appears in the left and right side (circled) of the figure..

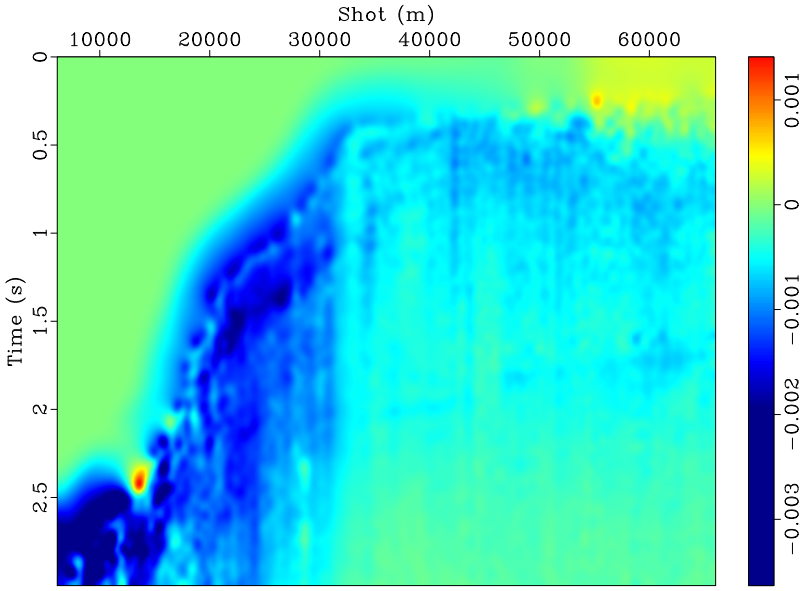

(a)

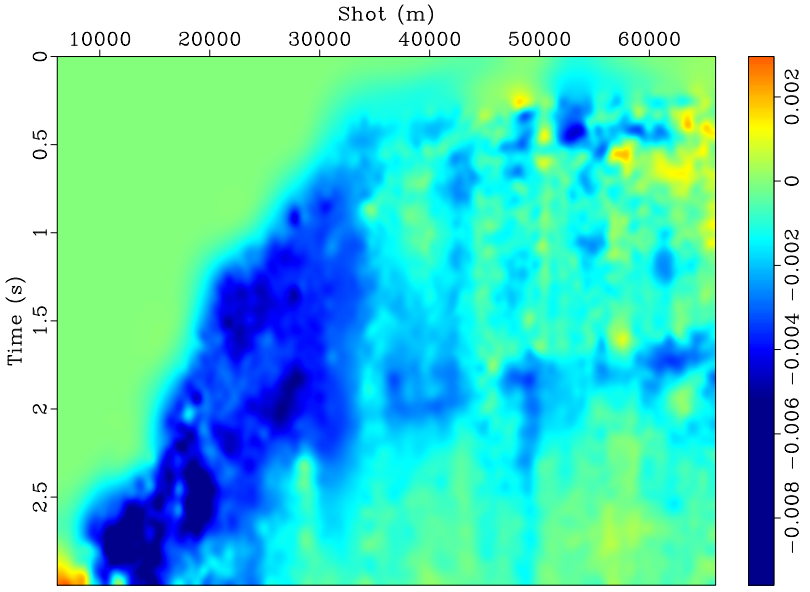

(b)

Figure 3.9: Variation of filter coefficients for near-offset data. Zero-lag coefficients (a). Mean of filter coefficients variations (b). The variations in the left part of the figure indicates that there is a difference between the predicted and real mutliples and the filter attempts to correct for the difference.

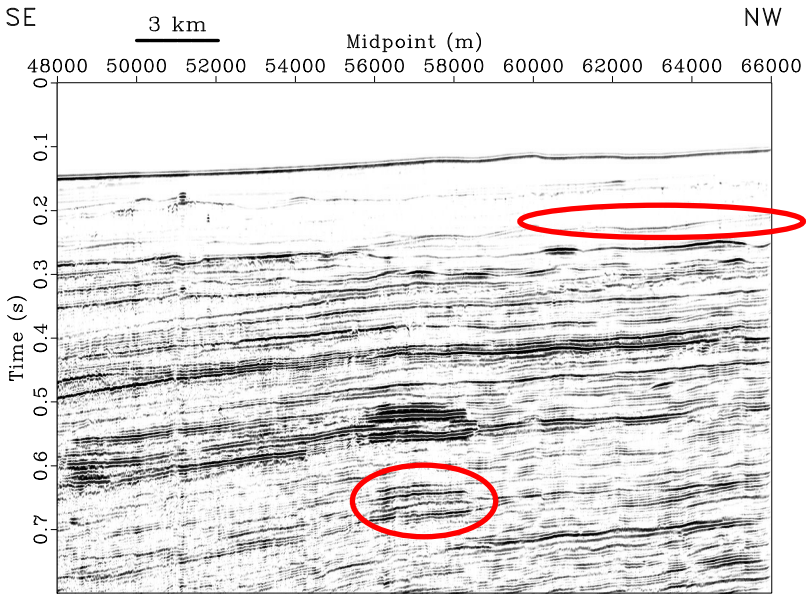

(a)

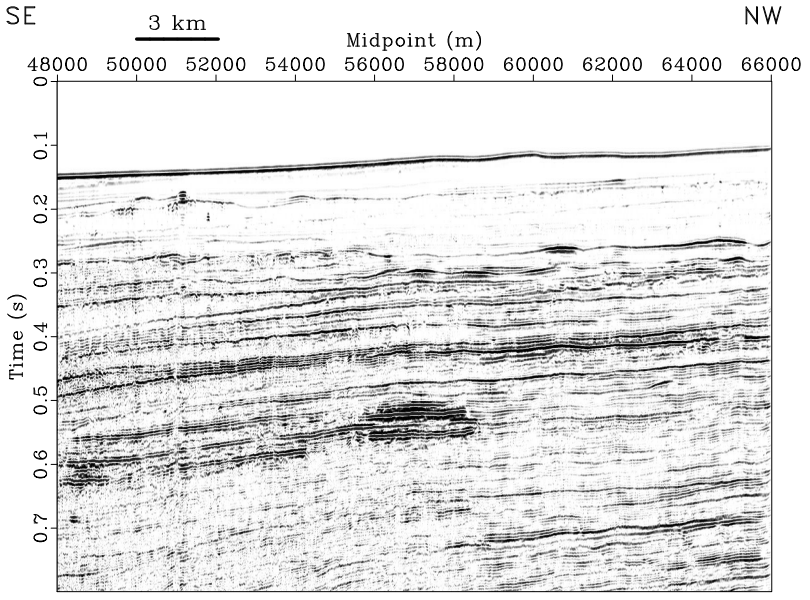

(b)

Figure 3.10: An area of the DMO stacked section corresponding to a shallw water depth. Before multiple attenuation (a). After multiple attenuation (b). The circled part shows the good muliple attenuation results.

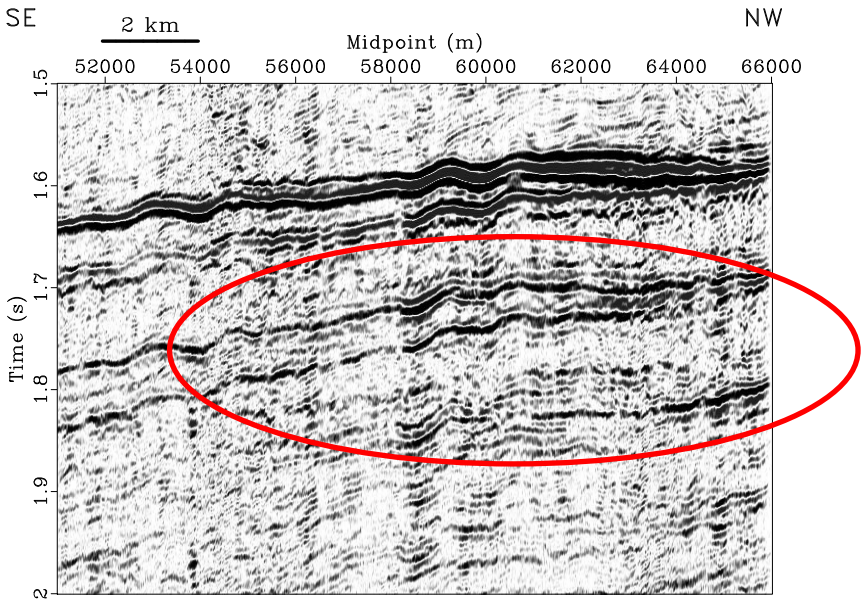

(a)

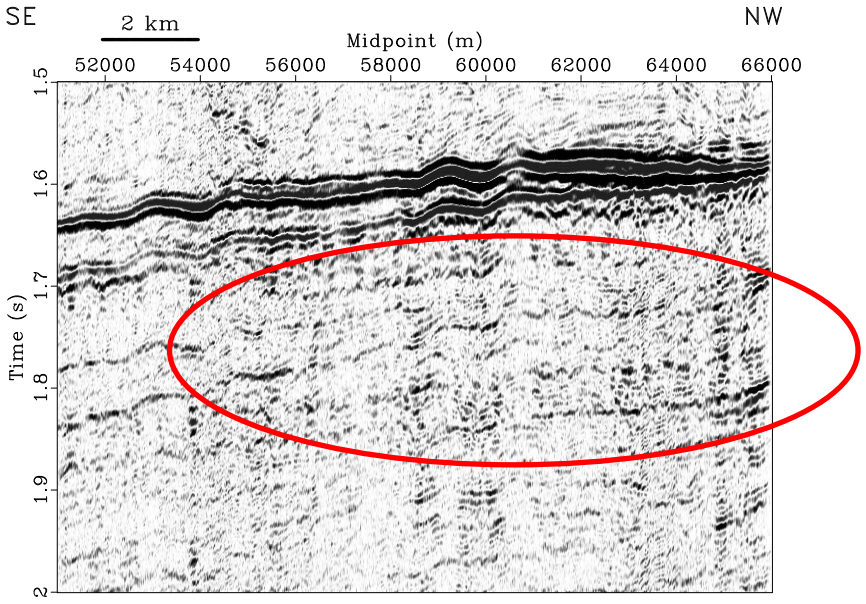

(b)

Figure 3.11: An area of the DMO stacked section before multiple attenuation(a) and after multiple attenuation (b). The peg-leg multiple (circled) is also attenuated.

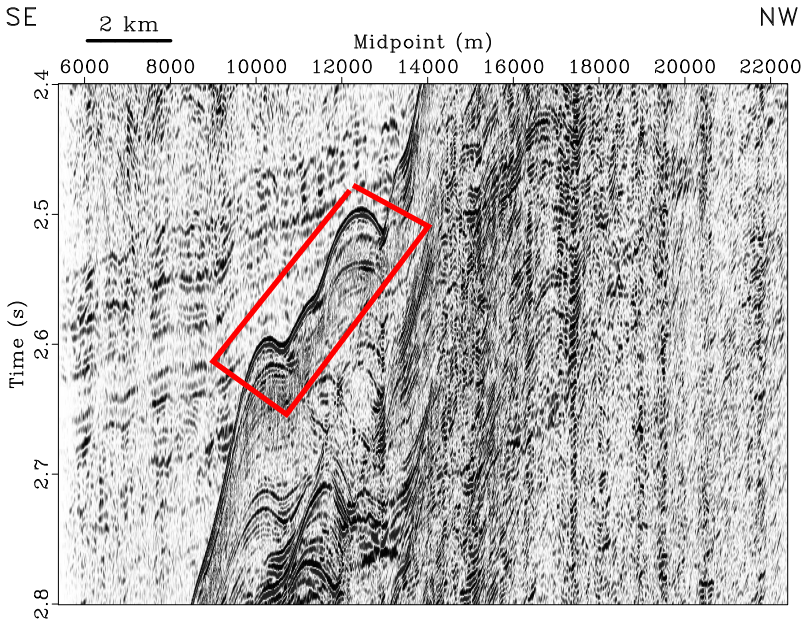

(a)

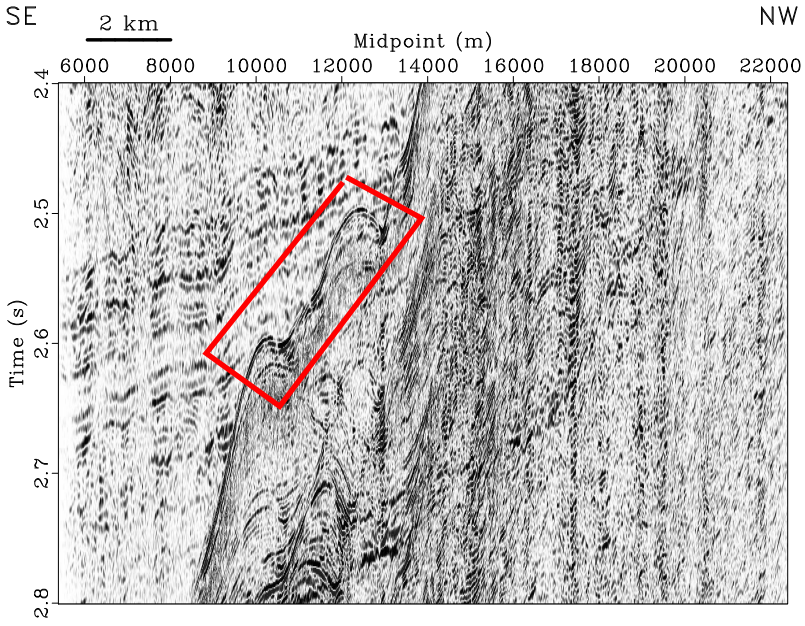

(b)

Figure 3.12: An area of the DMO stacked section before multiple attenuation (a) and after multiple attenuation (b). The multiple energy in this area comes from the dipping sea floor and was not attenuated but only reduced. Shown is a reduced strong multiple event (circled).

to be present in the dataset. Moreover, I chose not to alter the amplitudes of the data. A possibility of either destroying diffractions if the amplitudes of the data were adjusted, for example by running a mean filter, or diffraction multiples could not be predicted and potentially not attenuated.

The quality of adaptive filtering results depends on the quality of the predicted multiples, and the length of the filter coefficients. The closer the predicted multiples are, the better the result of the adaptive filtering. Also the longer the filter, the better the results of adaptive filtering. However, the computation cost in terms of memory usage and running time increases with the length of the filter.

Chapter 4

Diffractions separation using plane-wave destruction

Introduction

The goal of seismic imaging is to obtain the maximum possible resolution of subsurface structure (Yilmaz, 2001). This resolution comes from defining boundaries between layers and often discontinuous features. There are several challenges to achieve the maximum resolution. For one there is a limitation imposed on the size of resolvable objects by the frequency bandwidth of the seismic wavelet as approximated through Rayleigh's criterion - the size of resolvable object is 1/4 wavelength of the seismic signal. Moreover, conventional images are produced using seismic data processing processes designed to image reflection energy that comes from specular reflectors. In addition, the analysis performed on conventional images such as coherence analysis (Gersztenkorn and Marfurt, 1999) is susceptible to numerical artifacts and limitations in our knowledge of migration velocity in the migration process (Khaidukov et al., 2004; Moser and Howard, 2008; Landa, 2009). Figure 4.1(a) shows a synthetic earth model with a graben and a syncline, which I reproduced after Moser and Howard (2008). Figure 4.1(b) shows the zero-offset reflection response, while Figures 4.1(c) and 4.1(d) show the results of time migration using the correct imaging velocity and an erroneously low migration velocity, respectively. Observe that, with lower migration velocity, a discontinuity appears in the middle of the syncline, which demonstrates the effect of migration velocity error on analysis in the image space.

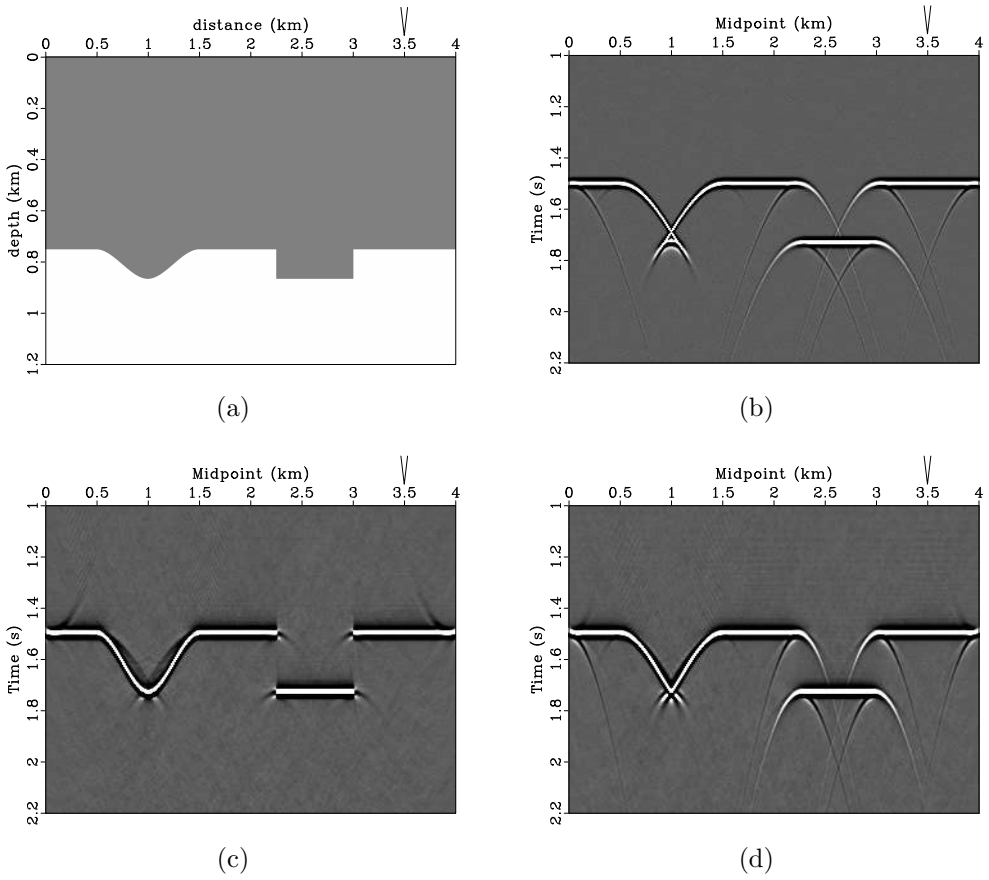

Figure 4.1: Earth model (2d profile) with a graben and a syncline (a). Zero-offset reflection response (b). Time migrated version of the reflection response with correct imaging velocity applied (c). Time migrated section with imaging velocity lower than the correct velocity (d). This illustrates the sensitivity of the imaging process to the errors in velocity. (Moser and Howard, 2008) using time migration rather than depth migration. The vertical arrow at 3.5 km shows the location of a CMP gather discussed later in this discussion.

An alternative approach for locating small discontinuities in the subsurface is to analyze diffraction energy. Diffraction energy comes from small objects (on the order of a wavelength) that scatter seismic energy. Diffraction energy analysis, thus, is suitable for describing small features in the subsurface . In fact, in the offset domain, specular reflections can be interpreted as infinitely many diffractors or Huygens' secondary sources. In this case, the diffracted energy is summed constructively and becomes reflection energy (Yilmaz, 2001; Moser and Howard, 2008). This idea is illustrated in Figure 4.2 which comes from a synthetic model reproduced after Moser and Howard (2008) - a similar model also appears in Yilmaz (2001). Figure 4.2(a) shows the zero offset seismic response for an earth model with a reflector that has sharp edges at the end and a (small discontinuity) fault in the middle (Figure 4.2(b)). The reflection energy appears from the main reflection while the diffraction energy (hyperbolic response in the offset domain) appears from the fault in the middle and also the edges of the reflector. Figure 4.2(c) and Figure 4.2(d) illustrate that the diffraction energy is not summed constructively when spacing between the diffracting points is increased to 0.240 km. Figure 4.2(e) and Figure 4.2(f) show the zero-offset data and its corresponding earth model for 3 diffractors which further explains the idea.

Diffraction energy has physical properties different from specular reflection energy (Klem-Musatov, 1994). Diffractions appear in the offset domain of seismic data as hyperbolas with their apex located at the scatterer and curvatures that decrease as a function of a diffractor depth (Sheriff, 2002). Additionally, diffraction energy has a weaker amplitude than reflection energy (Trorey, 1970). In fact, curvature also decreases as a function of source-receiver offset as I will show later that DMO corrects for this phenomena. Diffraction energy also presents a phase change at the edge of

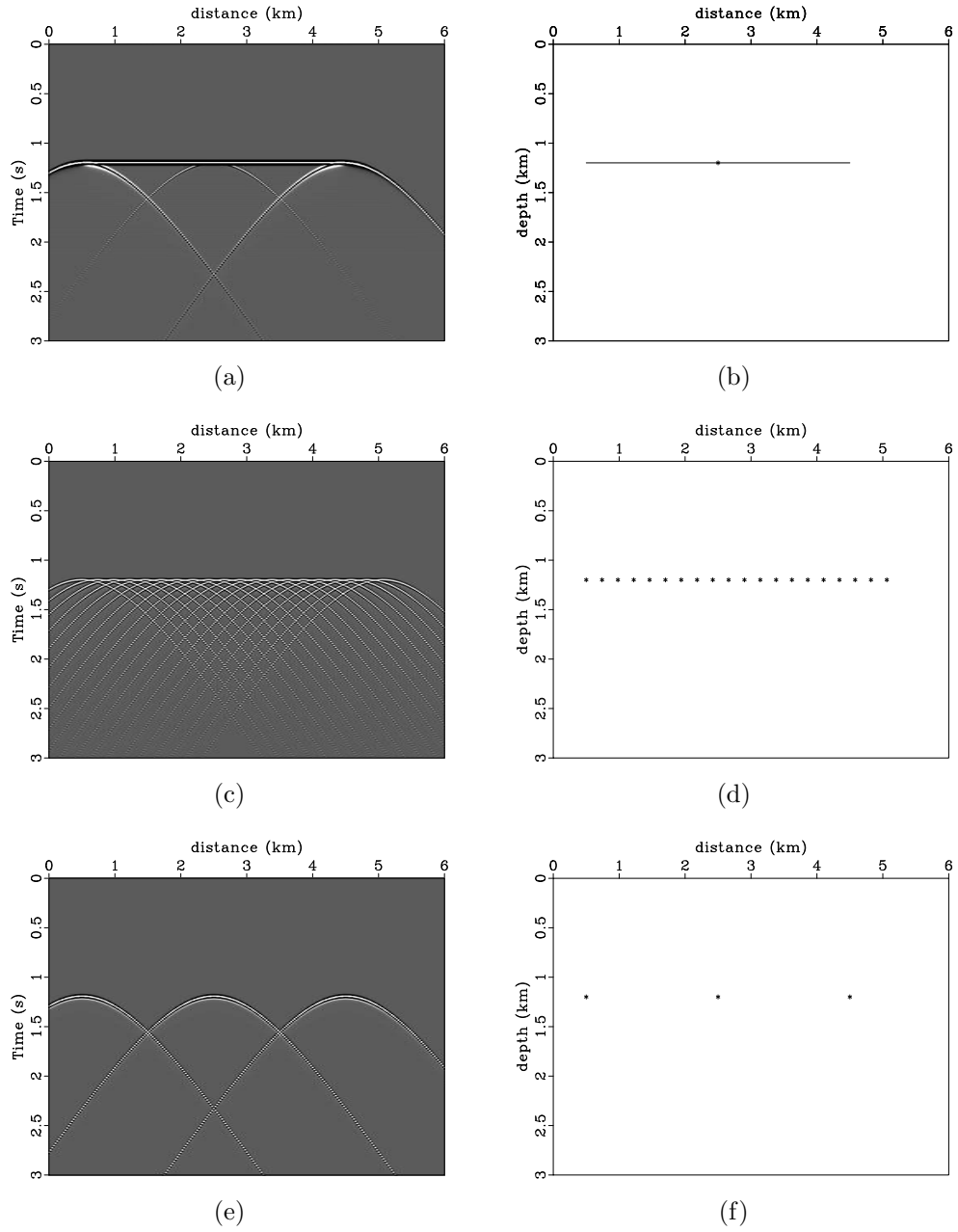

Figure 4.2: specular reflection with finite boundaries (a-b). Closesly spaced diffractors (c-d). Sparcely spaced diffractors (e-f). Notice the transition from specular reflection to the point scatter which illustrates that constructive interference of diffraction energy creates reflection energy. The model was reproduced after (Moser and Howard, 2008).

a reflector (Sheriff, 2002; Trorey, 1970). To demonstrate these properties, I created a synthetic earth model (Figure 4.3). Figure 4.3(a) depicts two horizontal reflectors at two different depths, each has two sharp edges. The zero-offset data are shown in Figure 4.3(b). One may notice that in the zero-offset domain, at any endpoint of the reflection, there is a diffraction where the amplitude decreases to 1/2 of the reflection amplitude (Trorey, 1970). The diffraction also shows a phase difference between the tails of the diffraction. In addition, it is shown that the curvatures of diffractions decrease as a function of diffrcators depth (Sheriff, 2002).

Diffraction imaging has recently gained attention in seismic data processing (Khaidukov et al., 2004; Fomel et al., 2007; Moser and Howard, 2008). This kind of seismic response naturally describes geological discontinuties such as small-scale faults, pinch-outs, and fracture terminations which are often the aim of interpreters (Trorey, 1970; Klem-Musatov, 1994; Khaidukov et al., 2004; Moser and Howard, 2008). Diffraction imaging also provides an analysis tool for Migration velocity estimation. The focusing of diffractions is used as a measure of the precision of migration velocity estimation. More details about migration velocity analysis using diffractions are discussed in the next chapter. Diffraction imaging is commonly done by separating diffraction energy from reflection energy. The separation is either applied in the image space (Landa et al., 2008; Klokov et al., 2010). An example, is separating diffractions from reflection using a hybrid Radon Transform for migrated data in the dip-angle domain where refelctions and diffractions have different geometrical shapes, as demonstrated by Klokov et al. (2010).

Diffraction separation may also be performed in the data $t - x$ space (unmigrated data) based on the wave equation propagation (Harlan et al., 1984; Landa et al., 1987; Khaidukov et al., 2004; Fomel et al., 2007). For example, Harlan et al.

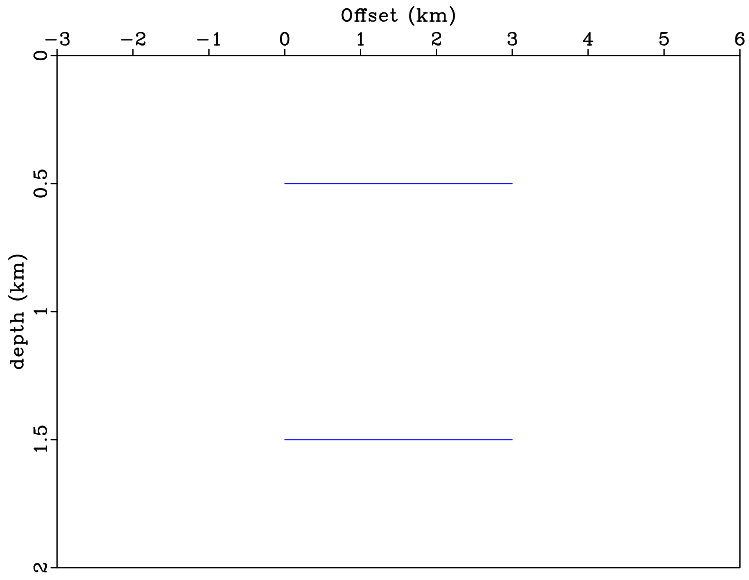

(a)

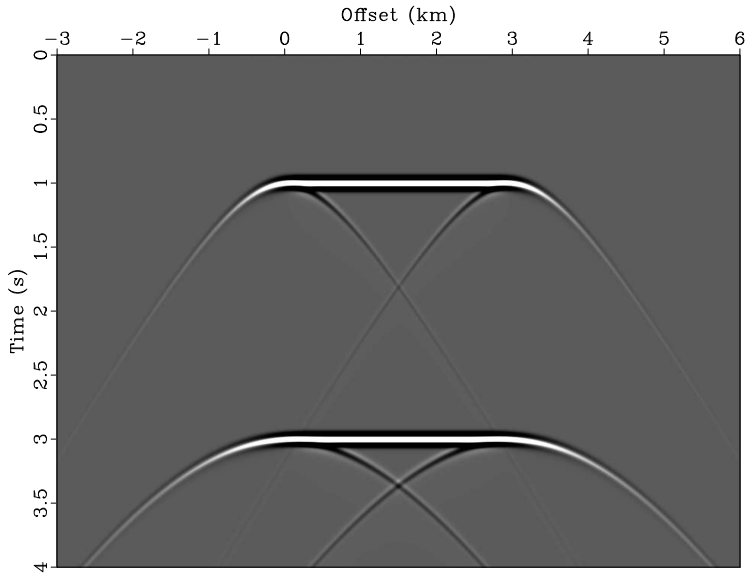

(b)

Figure 4.3: Earth model with two flat reflectors, each reflector ends with two sharp edges (a). Zero-offset data for constant velocity medium (b). Notice the decrease of diffractions curvature as the depth of the reflector increases. Also note that diffractions must undergo a 180° phase change on either side of a diffracting edge.

(1984), used a slant stack method to separate diffractions from reflection for data in zero-offset plane where reflections are continuous and coherent events. For small time windows, events are approximately linear and can be summed to a point in the slant stack space in which the points may then be deleted. Then applying an inverse slant stack, produces reflection events which can be subtracted from the original data. Khaidukov et al. (2004) suggested to separate diffractions by focusing reflection energy to their virtual source locations and muting those locations. Diffractions energy is then obtained by defocusing. Fomel et al. (2007) obtained diffraction images using plane-wave destruction method which predicts laterally continuous smooth events corresponding to reflection energy. The predicted reflection energy , thus, can be suppressed.

Next, I discuss requirements for diffraction imaging for poststack data processing using the synthetic dataset. Then, I present the plane-wave destruction (PWD) method for reflection energy suppression through synthetic models. After that, I show the results of applying PWD method on the field dataset from the Canterbury Basin.

Diffraction imaging for poststack data

Imaging diffractions for poststack data requires careful attention. The NMO correction is designed to move reflection times into zero-offset reflection time, but not correctly applies to the diffraction events (Moser and Howard, 2008). The idea was illustrated through the graben and syncline model (Figure 4.1). One NMO corrected CMP gather located at 3.5 km in the model (Figure 4.1(a)) is shown in Figure 4.4. This figure shows that the main reflection at time 1.5 s is correctly flattened by the NMO correction, while the 4 diffraction events "overcorrected". Consequently, summing data over offset after NMO correction causes diffractions to have "tails" as

shown in Figure 4.5(a). The figure clearly shows that NMO and CMP stack does not properly align diffractions, which have curvatures in the CMP gathered records decreasing as a function of source-receiver offset. The DMO operator, on the other hand, aligns diffractions and allows for a constructive sum. The DMO stack is shown in Figure 4.5(b) where diffractions are better aligned. Thus, the DMO corrected stack makes diffraction imaging for poststack data more effective.

Reflection Energy Suppression using PWD

Plane-wave Destruction (PWD) filters use a description of seismic reflection data based on the local plane-wave reflection model (Claerbout, 1992; Fomel, 2002). The local plane model is defined by the equation:

$$\frac{\partial P}{\partial x} + \sigma \frac{\partial P}{\partial t} = 0 \,, \tag{4.1}$$

where $P(t, x)$ is the wave field and σ is the local slope, which may also depend on t and x (Claerbout, 1992). Representing seismic data by a local plane-wave model allows one to conveniently perform many data processing steps. Fomel (2002) provided an improved finite-difference plane-wave destruction filter process. The improved finite-difference filters are alternatives to t-x domain filters. The application of the finite-difference plane-wave filters requires estimating the local slope dt/dx. Then, the plane-wave destruction filters are applied using the estimated slope. (Fomel, 2002) demonstrates the applications of plane-wave destruction filters in fault detection, data interpolation, and noise attenuation. Time domain imaging operators such NMO in the CMP gather domainare also possibly performed once the local slope is estimated from seismic reflection data. (Fomel, 2007).

Plane-wave destruction filters offer a convenient approach for extracting diffrac-

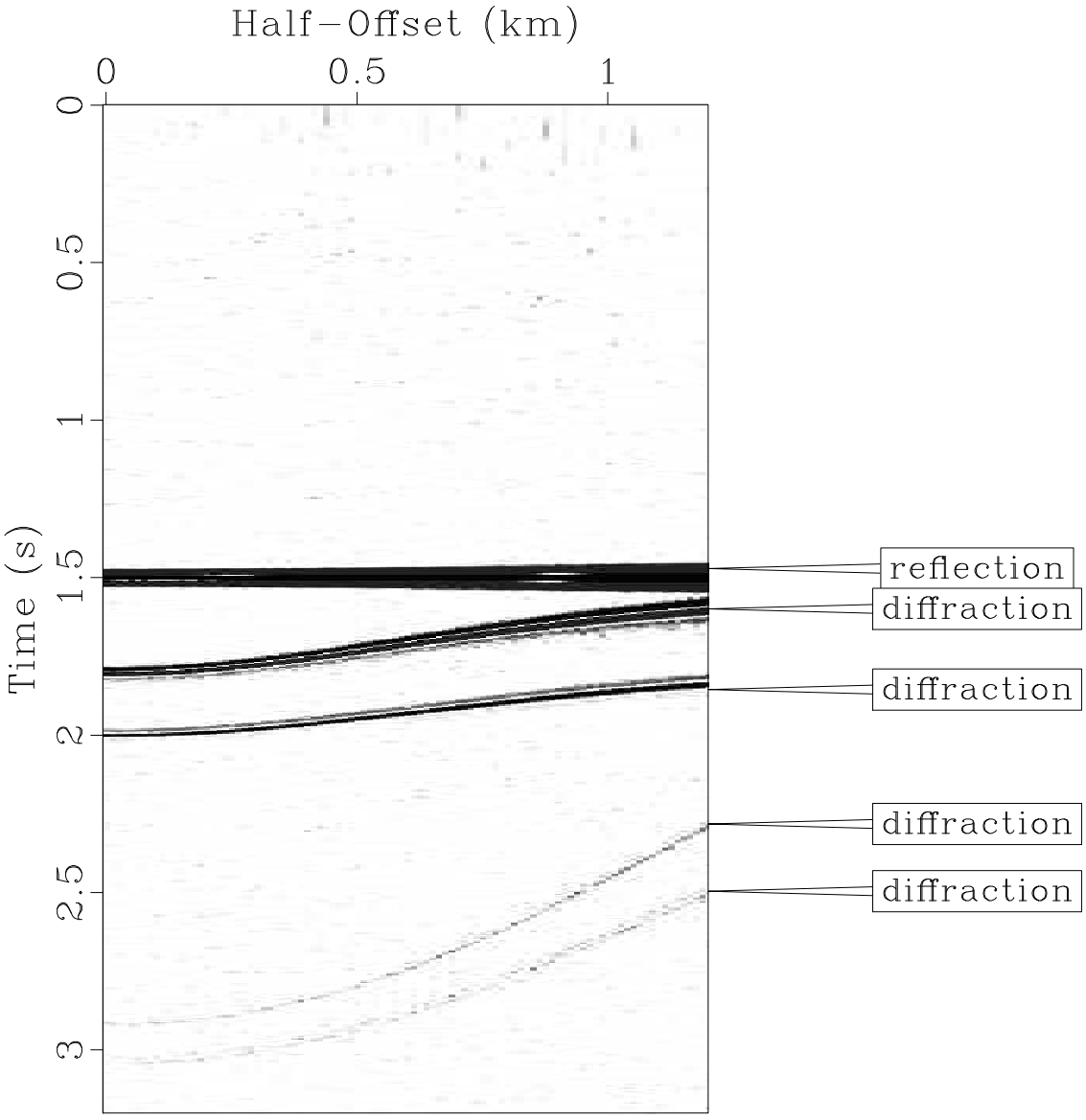

Figure 4.4: One NMO corrected CMP gather at location 3.5 km in Figure 4.1. Notice that the main reflection is correctly flattened by the NMO correction while the four diffraction events are not. Thus a sum of all these traces will corretly enhance the reflection event and diminish the diffraction events

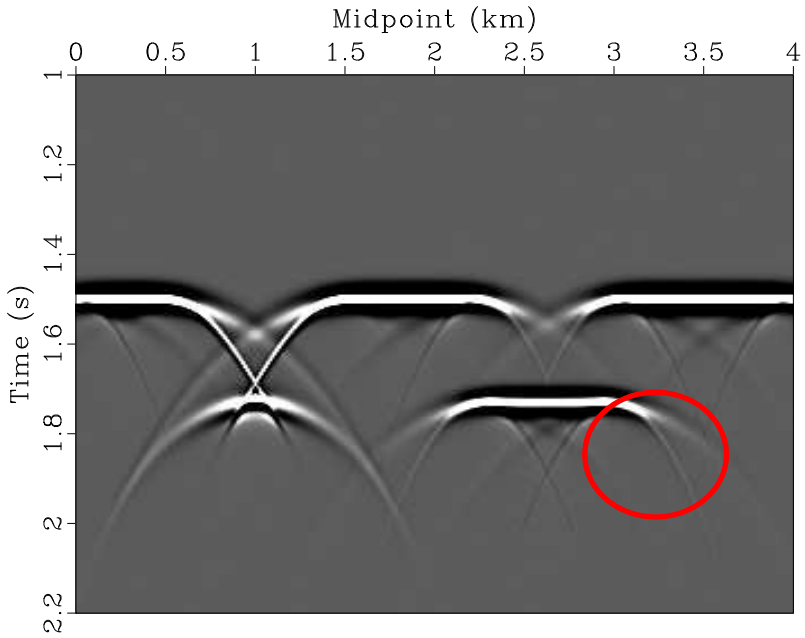

(a)

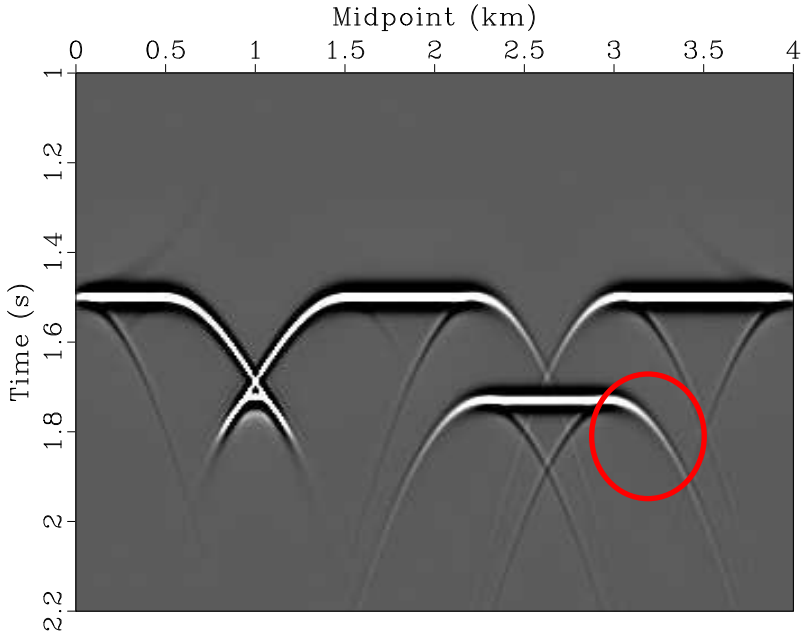

(b)

Figure 4.5: NMO corrected CMP stacked section (a). Notice the diffraction tails (circled) which are not aligned. DMO stacked section (b) aligns diffractions which makes diffraction imaging for poststack data more effective.

tions from seismic reflection data. Fomel et al. (2007) used plane-wave destruction filters to image faults, channels, and a salt body for poststack data. The key concept is that plane-wave destruction filters effectively predict the smooth, continuous events in the seismic data. Reflection energy in the offset plane of seismic CMP gathers volume generally appears as strong, smooth, and continuous events. Plane-wave destruction filters, thus, naturally predict and suppress this specular reflection energy (Fomel et al., 2007). The remaining data should contain other kinds of coherent seismic energy such as diffraction energy, and random noise. Diffraction energy in the offset domain of reflection-free data appears as coherent hyperbolas, which makes it different from random noise.

Synthetic Examples

I illustrate the diffraction separation by the plane-wave destruction method using two synthetic models. The first model is the one with a graben and a syncline from Moser and Howard (2008) which is shown in the structural profile shown in Figure 4.1(a). The estimated local slopes using the plane-wave destruction method from the DMO corrected stack (Figure 4.5(b)) is shown in Figure 4.6(a). The separated diffractions are shown in the structural profile in Figure 4.6(b). The weak diffraction energy is effectively extracted. The triplication response from the syncline (small radii of reflection curvature) would be included in the diffraction separated data. Figure 4.6(c) shows the migrated diffractions. The diffractions are focused into their apexes. In contrast, the triplication from the syncline may be mis-interpreted as diffraction migrated with low velocity. Therefore, both migrated conventional and diffraction images are necessary for complete geological interpretations of seismic data.

The second synthetic model has one curved reflector and 4 buried diffractors at the depth of the reflector (Figure 4.7(a)). I applied the plane-wave destruction method on the simulated zero-offset data (Figure 4.7(b)). The zero-offset data shows the specular reflection as strong, continous, and smooth event while the diffractions response from each diffraction point is hyperbolic. The estimated slope using the plane-wave destruction method for the zero-offset data is depicted in Figure 4.7(c). The slope estimation parameters were chosen to predict the reflection energy effecively. The slope shown in the figure follows the reflection event slope. Then, the estimted slope is then used to subtract the reflection data from the zero-offset data. The separted reflection data is shown in Figure 4.7(d) in which the diffraction energy appears reduced when compared to the one in Figure 4.7(b). The separated diffractions are shown in Figure 4.7(e). The reflection energy suppression was effective. The separated diffractions (Figure 4.7(e)) are then migrated as shown in Figure 4.7(f). This figure only shows 4 diffracting objects. These objects were distinguished from the main reflector (Figure 4.7(b)).

Seismic Field Data

First I further emphasize the importance of applying DMO to diffraction data in the poststack domain. Figure 4.8(a) shows the diffraction response for NMO corrected CMP stack. Figure 4.8(b) shows diffraction response for DMO stack. The diffractions in the NMO stack (circled in the figure) have tails that are not aligned. That is because diffraction curvature decreases with source-receiver offset and NMO operator does not correct for this phenamena. Summing NMO corrected diffraction data causes diffractions to have unaligned tails. On other hand, The second figure clearly shows enhanced aligned diffraction energy (circled in the figure). DMO oper-

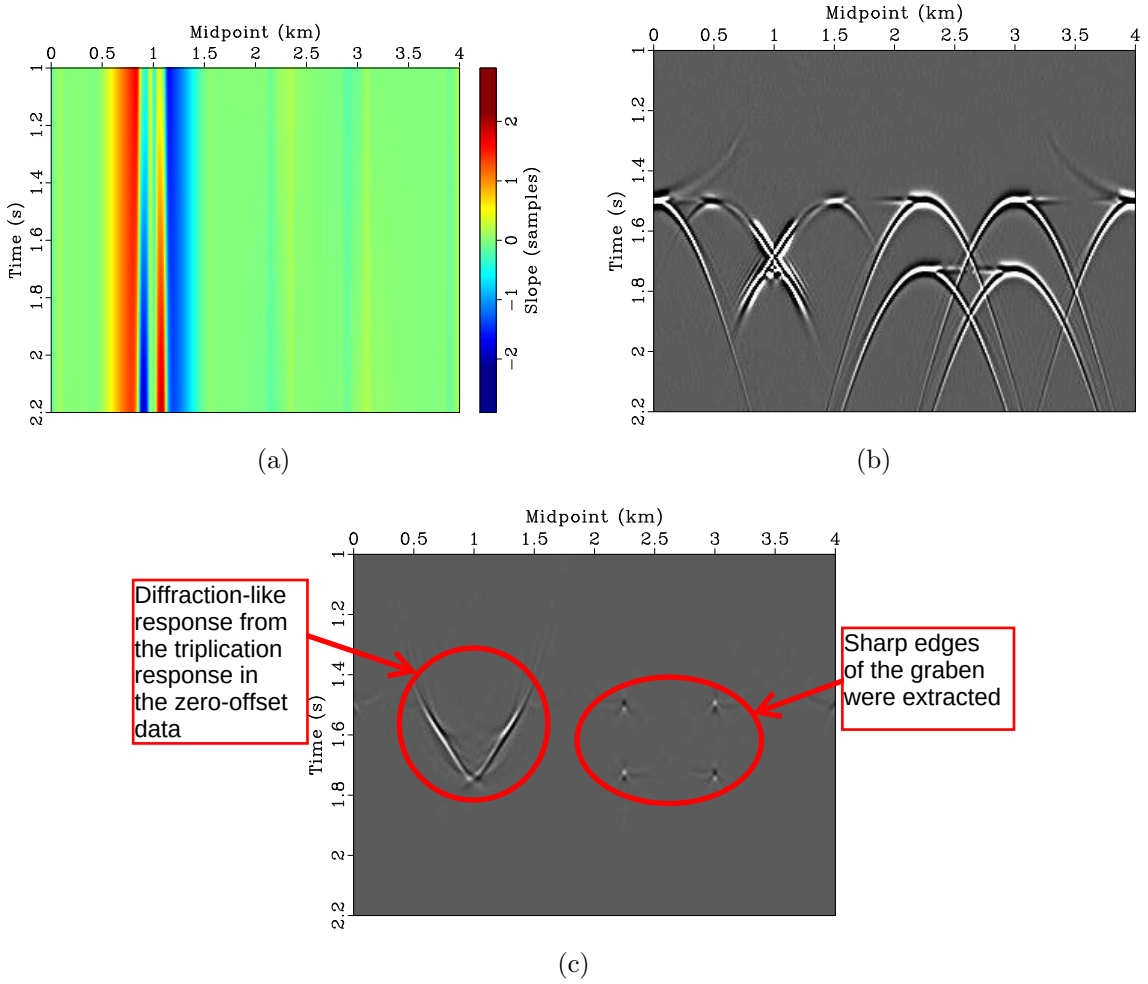

Figure 4.6: Dominant slope estimated for NMO corrected CMP stacked profile using plane wave destruction method (a) for DMO stack data for the model in Figure 4.1(a). Separated diffractions (b). Migrated diffractions with correct velocity (c). Triplication in the diffraction migrated section from the syncline can be mis-interpreted as a diffraction.

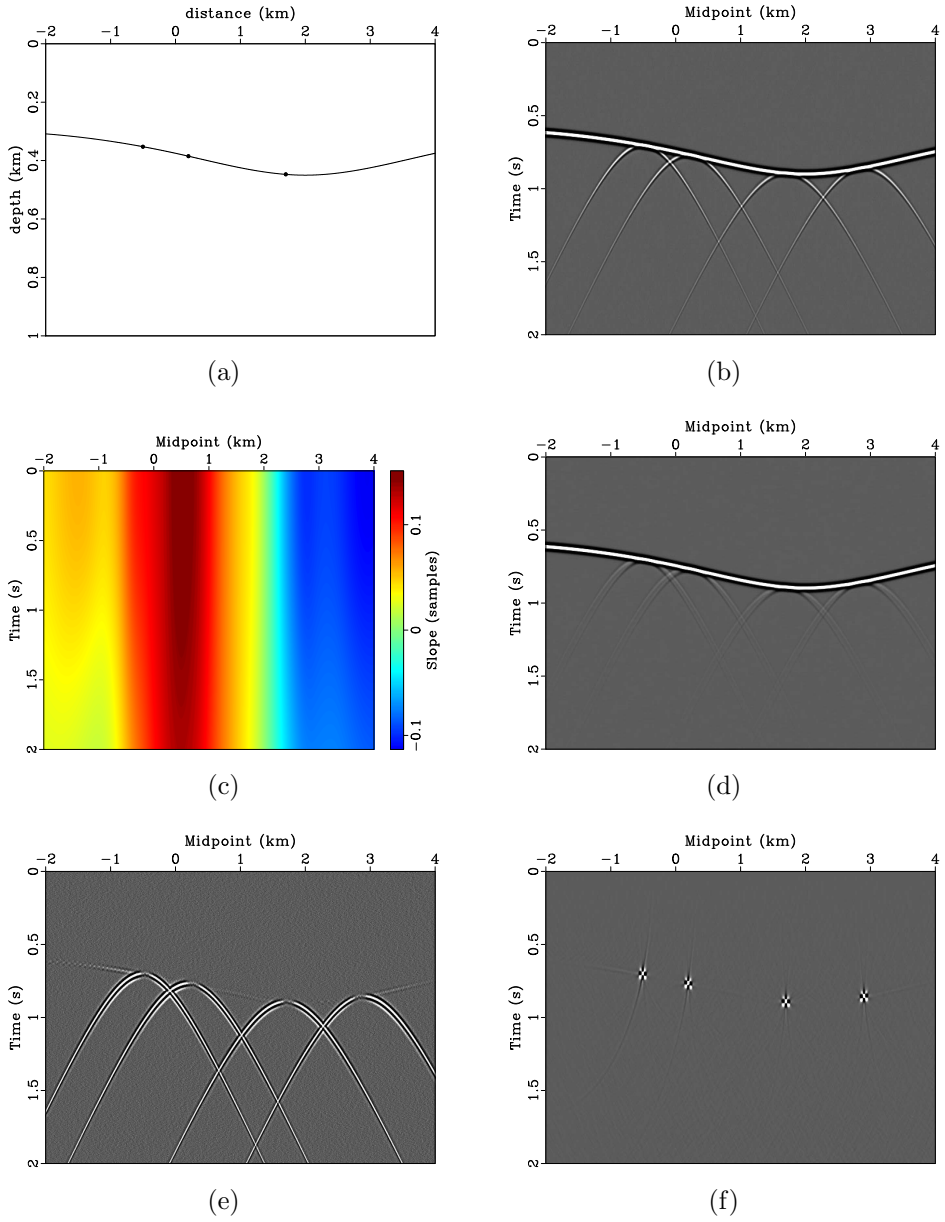

Figure 4.7: Synthetic earth model that has one non-horiozontal reflector and four diffractors located near the reflector (a). Zero-offset reflection response for the model (b). Predominant slope estimated using plane-wave destruction method (c). Separated reflections (d). Separated diffractions (e). Migrated diffractions with correct velocity (g). The plane-wave destruction method effectively suppressed specular reflection energy and allowed for locating buried diffractors.

ator moves diffractions to zero-offset and thus adjust their curvatures. Due to their weak energy diffractions are dominated by reflection energy and may not easily be noticble unless they are separated.

I applied the plane-wave destruction method on the DMO stacked section. Figure 4.9 show the dominant slope estimated using the plane-wave destruction filters and the extracted diffraction section, respectively. Comparing the conventional DMO stack (Figure 4.8(b)) to the diffraction stack (Figure 4.9(b)) clearly shows that plane-wave destruction method is capable of suppressing reflection energy. Moreover, hidden diffractors are illuminated quite effectively in the diffraction stack.

Discussion

I applied diffraction separation using the PWD method on synthetic data (for testing and illustration purposes) and the Canterbury dataset from Line 12. Although diffraction energy is weak, PWD can enhance it by predicting and suppressing reflection energy. In the common-offset domain, diffraction separation is more attractive. Even though PWD separates diffractions in the data space, there exist areas where diffraction-like response will appear. Consequently, one needs to look at both conventional and diffraction images. The diffraction response from reflections of small radii curvatures, on the other hand, could be another tool for interpreters (Sava et al., 2005). In fact, this kind of response provides possible explanation for a similar response present in the diffraction image of line 12 as we will see in the next chapter.

Another aspect of diffraction separation using plane-wave destruction method is that reflection multiples are possibly suppressed during diffraction separation step. Multiple reflections in the offset domain resemble primary reflections - smooth and

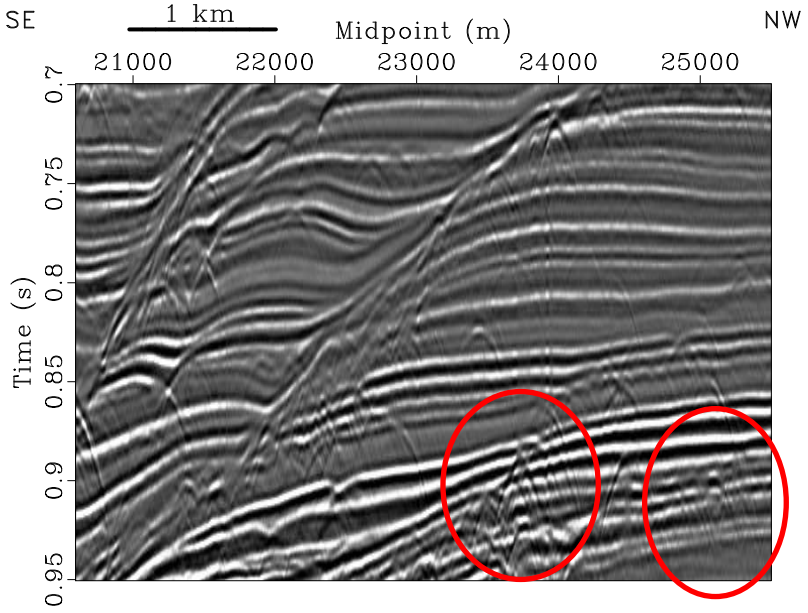

(a)

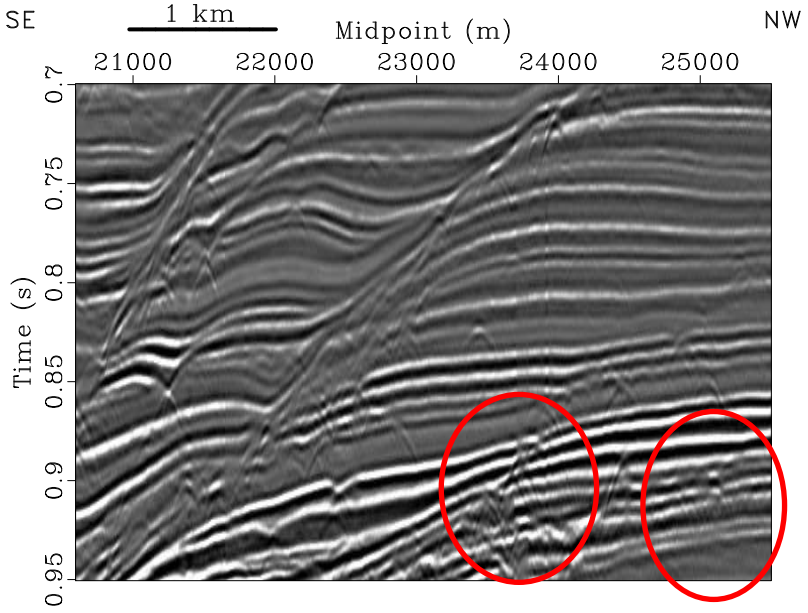

(b)

Figure 4.8: NMO stack (a) diffractions (circled) appear with several tails due to the curvature dependence on offset. DMO stack (b) diffractions (circled) are aligned. DMO accounts for the change in curvature of diffractions and properly moves them to zero-offset data.

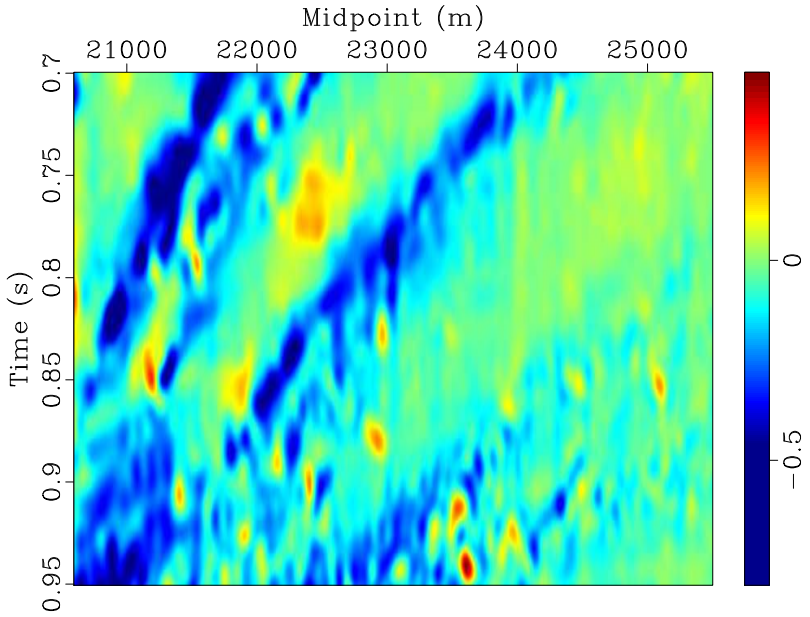

(a)

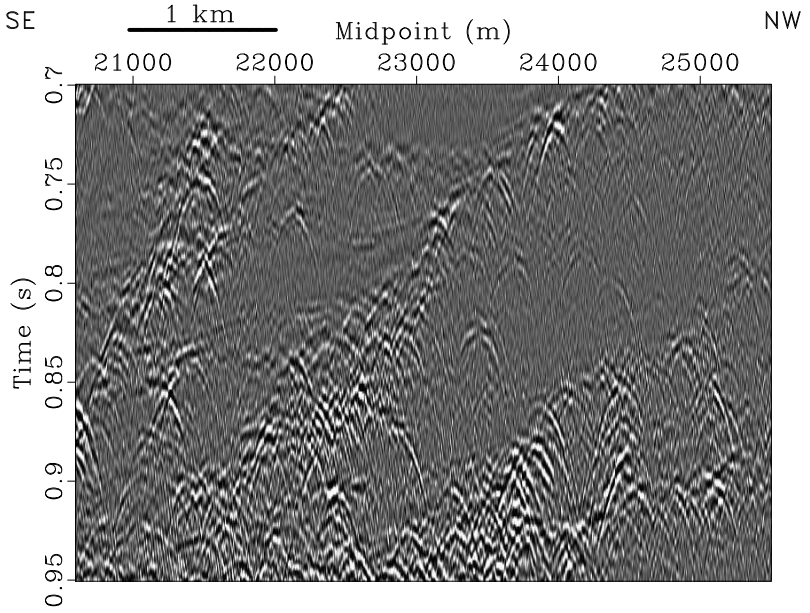

(b)

Figure 4.9: Dominant slope (a) for DMO stacked section shown previously in Figure 4.8(b). The slope estimation follows the specular reflection energy effecively which allows for their subtraction. Extracted diffractions (b) after reflection suppression using the estimated slopes by the plane-wave destruction. The diffractions appear hyperbolic in this DMO stacked profile.

laterally continuous events. However, the diffraction multiples may still be present in the separated diffractions data.

Chapter 5

Migration of diffractions in the dip-angle domain

Introduction

Migration is a major step in seismic data processing workflow. Migration increases temporal resolution by collapsing diffractions and moving reflection events into the structural position of reflectors in the subsurface (Yilmaz, 2001; Biondi, 2006). Ideally, migration techniques need to handle steep dips, vertical and lateral velocity variations. Migration is generally achieved by two different classes of techniques: Integral-based methods or wave-equation methods (Yilmaz, 2001; Biondi, 2006). Integral-based methods are referred to as Kirchhoff migration in which traveltime is computed explicitly for a range of possible propagation paths. The reflection amplitudes, after applying amplitude and phase corrections, are summed over a diffraction hyperbola whose curvature is defined by propagation velocity in the medium (Schneider, 1978). Integral-based methods can handle dips up to 90 degrees, but not strong lateral velocity variations. Integral-based method could be further categorized depending on the description of the vertical axis as Kirchhoff time migration or Kirchhoff depth migration. Time migration, where the vertical axis is two-way traveltime, has some advantages of working with an approximated velocity model while depth migration, where the vertical axis is depth, requires more accurate interval velocity model but produces more accurate results. Integral methods tend to be more intutive than wave-equation methods, but are computationaly intensive.

Wave-equation methods, on the other hand, are based on wavefield continuation (Claerbout, 1971; Claerbout and Doherty, 1972). Wave-equation methods are further categorized as those based on a one-way wave propagation and two-way wave propagation. The one-wave wave-equation propagates the wavefield in depth. The idea is to extrapolate wavefields from the surface to the subsurface and apply an imaging condition. The imaging condition states that the reflector shape corresponds to the extrapolated wavefield shape at the time of reflection. The two-way wave-equation methods, on the other hand, propagate the wavefield in time and normally referred to as Reverse Time Migration (RTM). The imaging condition, in this case, is the cross-correlation between the upgoing and downgoing wavefields (Claerbout, 1971). Wave-equation methods can produce more accurate results than the integral-based methods, but they are computationally more expensive.

One important assumption for migration methods to perform well is the availability of precise migration velocities. There are several approaches to estimating migration velocities. For prestack data, offset-domain common image gathers (ODCIG) are typically used for migration velocity estimation. When Kirchhoff methods are used to generate the ODICG, flat image gathers indicate correct migration velocities. In contrast, focused image gathers indicate correct migration velocity for the ODCIG generated by wave-equation methods. The traditional ODCIG approach, however, suffers from multipathing effects. Prucha et al. (1999) present a simplified explanation where one reflection event element in the data space may correspond to more than one reflector element in the image space. Angle-domain common image gather (ADCIG) alleviates the multipathing problem (Prucha et al., 1999; Sava et al., 2005). Both Kirchhoff (integral) and wave-equation methods generate ADCIG in which the images are sorted by incidence angle at the reflection point. In this case,

flatness of the events is used a criterion for migration velocity analysis.

Unlike ODCIG and ADCIG which work with prestack data, diffractions, which are sensitive to migration velocity, provide a tool for migration velocity analysis for poststack data. For example, focusing of diffractions in CMP stacked data provides a measure for migration velocity analysis (Sava et al., 2005; Fomel et al., 2007). Another example of velocity estimation, is using the flatness of diffractions in the dip-angle gather images for migration velocity analysis (Landa et al., 2008; Reshef and Landa, 2009).

Kirchhoff time migration in the angle-gather domain produces good results for simple structural situations. In addition, time migration is also favored by interpreters because it is easy to relate migrated and unmitigated sections in order to evaluate the efficacy of migration process. I briefly describe Kirchhoff time migration in angle gather domain. Then, through a synthetic dataset, I illustrate the velocity continuation and path-integral methods for migration velocity analysis using diffraction data. I follow this by generating both a conventional image and a diffraction image using Kirchhoff migration in the dip-angle gather domain for the Canterbury dataset.

Kirchoff Migration in the dip-angle gather domain

Angle-gather migration generates images grouped by angle of incidence at the reflection point. There are several advantages of angle-gather migration such as velocity analysis or Amplitude variations with Angle (AVA) analysis. Fomel and Prucha (1999) presented a formulation of angle-gather time migration that produces images in open-angle and dip-angle gathers domain. One advantage of this approach

is the separation of diffractions and reflections in the image space (Landa et al., 2008). Another is the ability to use diffraction flatness as a measure for migration velocity analysis for poststack data (Landa et al., 2008).

Figure **??** shows the raypath in constant velocity medium where s is the shot, r is receiver, γ is the reflection or opening angle (angle between the ray and the normal to the reflector), and α is the dip angle (as well as the emergence angle at the surface). Based on this figure, Fomel and Prucha (1999) define the kinematic of angle-gather migration by the following equations:

$$t = \frac{2\,z}{v}\,\frac{\cos\alpha\,\cos\gamma}{\cos^2\alpha-\sin^2\gamma} \tag{5.1}$$

$$h = z\,\frac{\sin\gamma\,\cos\gamma}{\cos^2\alpha-\sin^2\gamma} \tag{5.2}$$

$$x-\xi = z\,\frac{\sin\alpha\,\cos\alpha}{\cos^2\alpha-\sin^2\gamma} \tag{5.3}$$

And the inverse transformation from t, h, and $x-\xi$ to z, γ, and α:

$$z^2 = \frac{[(v\,t/2)^2-(x-\xi)^2]\;[(v\,t/2)^2-h^2]}{(v\,t/2)^2} \tag{5.4}$$

$$\sin^2\gamma = \frac{h^2\;[(v\,t/2)^2-(x-\xi)^2]}{(v\,t/2)^4-h^2\,(x-\xi)^2} \tag{5.5}$$

$$\cos^2\alpha = \frac{(v\,t/2)^2\;[(v\,t/2)^2-(x-\xi)^2]}{(v\,t/2)^4-h^2\,(x-\xi)^2} \tag{5.6}$$

where v is the medium velocity, and h is the source-receiver half-offset, z is the depth of the reflection, x is the midpoint, ξ is reflection point, α is the dip angle, γ is the reflection or opening angle, and t is the total reflection time.

Velocity Continuation and path-integral

Velocity continuation is a time-migration velocity analysis tool that propagates seismic images as a function of migration velocity (Fomel, 1994). In other words,

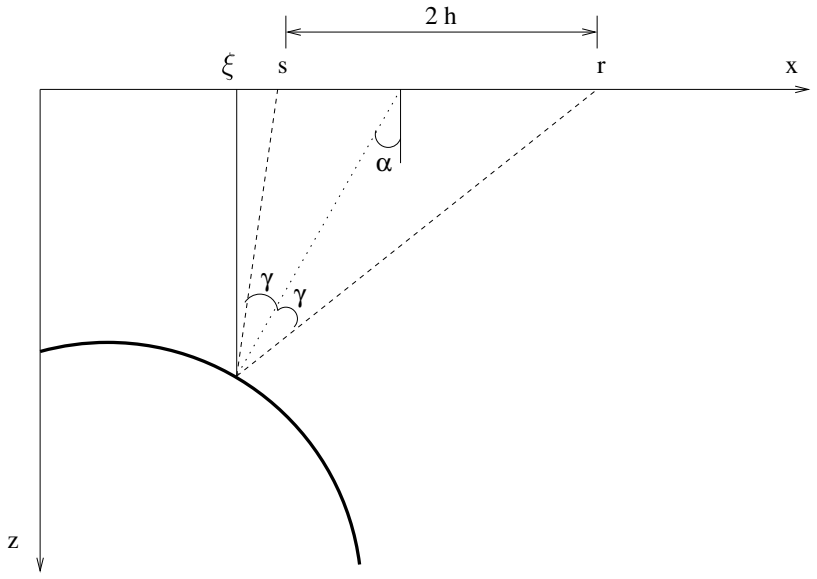

Figure 5.1: Reflection rays in a constant-velocity medium. s is the source position, r is the receiver position, γ is the angle between the ray and the nomral to the reflecting surface, α is the emergence angle at the surface, and ξ is the reflection point. Figure from(Fomel and Prucha, 1999).

velocity continuation describes the change in a seismic image as the migration velocity changes. Unlike other migration analysis tools, the velocity continuation method properly accounts for both vertical and lateral movements of events on seismic images. Velocity continuation also has applications in diffraction imaging (Fomel et al., 2007).

The velocity continuation method applied to diffractions is a promising method for migration velocity analysis. The method is the first of a two-step process in migration velocity estimation. The second step is about extracting the best image and and selecting the corresponding migration velocities. For instance, Varimax (inverse of a semblance of a squared of a function) was used by Fomel et al. (2007) to extract the best image and its corresponding velocities from the images created by velocity continuation (the first step). Another example is the integral-path method by Burnett

and Fomel (2011).

Landa (2004) introduced a path-integral formulation for seismic imaging. He proposed summing elementary signals over a sample of all possible paths between source and receiver obtained by different velocity models. Landa et al. (2006) extended path-integral imaging to include image-weighting functions for pre-stack imaging. Burnett and Fomel (2011) proposed a method based on similar principles with the premise that stationary points (apexes of diffractions) remain stationary regardless of the migration velocity used. Therefore, summing the set of images generated by velocity continuation preserves the apexes. In other words, stacking the set of images should cancel the tails of diffractions leaving only the apexes. This method is not optimal as I show with synthetic data, because residual reflections remaining in the diffraction data may contribute to the summation.

Synthetic data

To illustrate the velocity continuation and integral-path methods, I refer back to the synthetic model in Chapter 4 (Figure 4.7(a)- where we have four diffractors on a non-horizontal reflecting surface). The model was created with a constant velocity of 2 km/s. I applied velocity continuation on the zero-offset diffraction data extracted by the plane-wave destruction method using a range of 21 velocities incremented at 0.1 km/s and starting from 1 km/s. For a velocity range from 1-3 km/sec, a total of 21 images, each with different constant velocity, are created. Figures 5.2(a) and (b) show the images created with velocities 1.9 km/s and 2.1 km/s respectively. The first figure corresponds to image created with low velocity (5% below the correct velocity) and diffractions are concave down. Whereas the second figure shows the diffractions response (concave-up) to higher migration velocity (5% above the correct velocity).

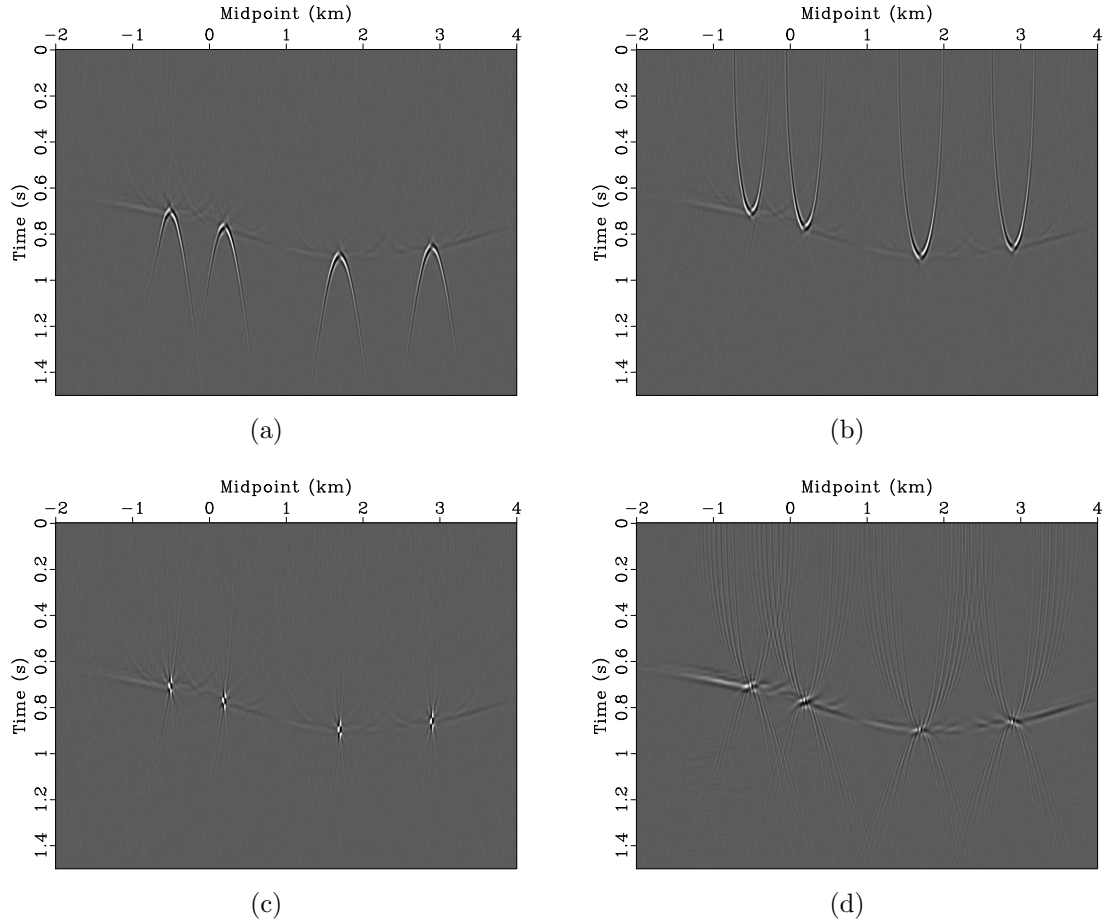

Figure 5.2: Velocity continuation method applied to the separated diffractions shown in Figure4.7(e). A total of 21 images for a range of 1-3 km/sec velocities were generated. Extracted image corresponding to 5%lower migration velocity (a). Extracted image corresponding to 5% higher migration velocity (b). An image that corresponds to the correct migration velocity (2 km/sec) (c). Image generated by summing (integral-path method) the 21 images (d).

The results of applying integral-path method is shown in Figure 5.2(d). Diffractions are focused into their apexes. One may also observe the presence of residual reflections in the image. Figure 5.2(c) shows the migrated diffractions using the correct velocity.

Seismic Field Data

I applied velocity continuation method on the extracted diffractions from the poststack Canterbury dataset using a range of 1400 m/s to 3500 m/s with an increment of 10 m/s. Figures 5.3 and 5.4 show the images created with velocity 1420 m/s and 2500 m/s respectively. In the first figure, the diffractions (circled in the figure) appear concave down. This response of diffractions for 1420 m/s migration velocity, which is lower than the water velocity, confirms to the results obtained for th synthetic experiment (Figure 5.2(a)). On the other hand, the next Figure 5.4, shows the diffractions concave up. The expected migration velocity at sea floor is around 1500 m/s, thus, migrating the diffractions at the sea floor higher migration velocity (2500 m/s) causes diffractions to concave up. The results in this figure also confirm to the results in the synthetic experiment (Figure 5.4).

The concave up events at the sea floor that appear in the three figures is possibly explained as reflections with small radii of curvature. The synthetic model used in Chapter 4 4.6(c) to illustrate the diffraction separation using plane-wave destruction method clearly reveals the response of a reflector with a small radii of curvature. Figure 4.6(b) shows a triplication coming from the syncline that will be present in the diffraction data and after migration, the event becomes concave up.

Once the range of images are created using velocity continuation, one needs to extract the focused image and its corresponding migration velocities. Integral-

path method states that the focused image is the summed images with the promise that diffraction apexes are stationary points and never change with velocity. I use the stacking velocity to create a mute to ensure that the summation is only created by reasonable velocity range. Then, I use the estimated migration velocity to migrate both the data before diffraction separation and after diffraction separation. Figure 5.5 shows the results of summing the 201 diffraction images, integral-path method. Diffraction energy appears more focused in the image. The idea is that the diffraction curvature in the image space depends on the migration velocity. The curvature of the diffraction increases as the migration velocity approximates the correct one. Therefore, diffraction tails of different curvatures cancel during the summation while the apex point remains intact.

Figures 5.8(a) and 5.8(b) show a conventional image and diffraction image from a portion of the field data. The second image shows the diffractors hidden in the conventional image. Small-scale faults are also illuminated. Another part of the line is shown in figures 5.9(a) and 5.9(b). Again the diffraction image reveals more subtle details in the subsurface that interest interpreters

Figure 5.10(a) shows one dip-angle gather from conventional image gathers which were generated by migrating the DMO stack in the dip-angle gather domain. While Figure 5.10(b) shows the corresponding dip-angle gather from diffraction image gathers of the migrated separted diffractions. The left figure shows the strong and dominating reflection energy concave-up. Whereas the right figure illuminates the diffraction energy. The different geometrical shapes of reflections and diffraction as shown in the two figures allows for diffraction separation in the image space, as demonstrated by Klokov et al. (2010)

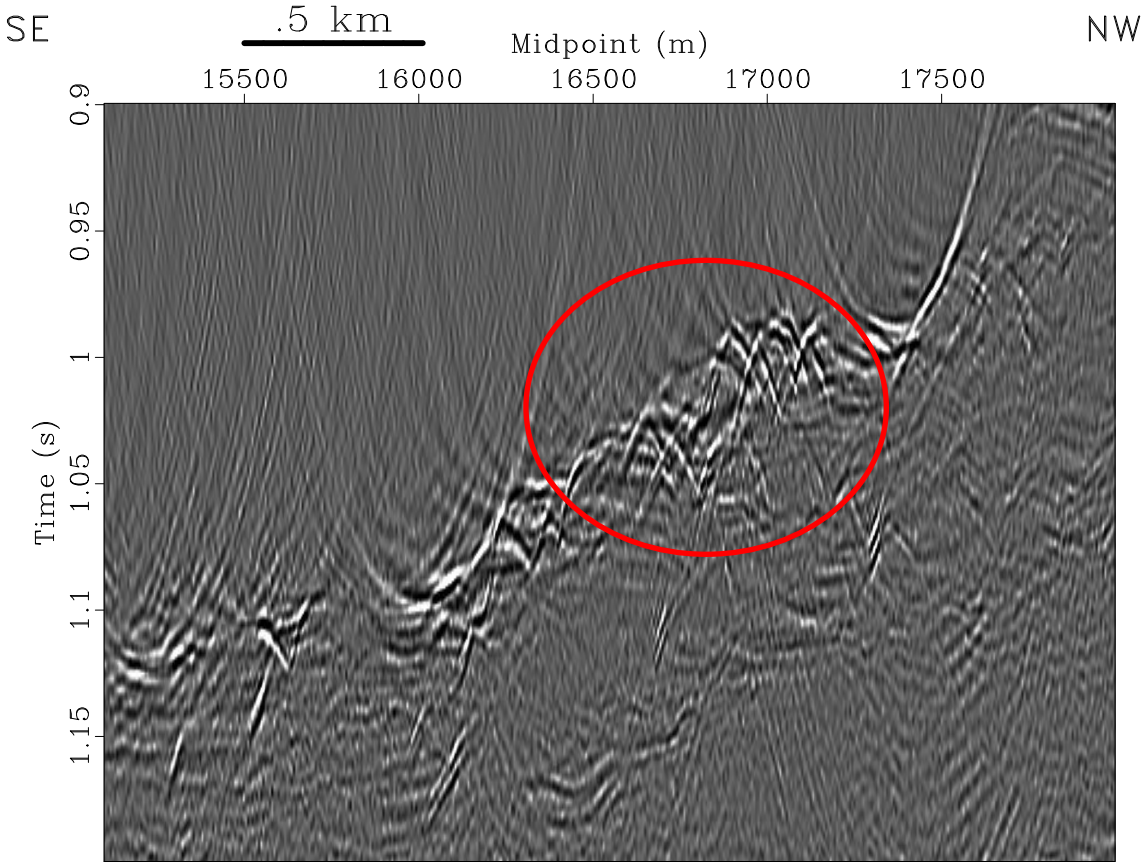

Figure 5.3: Extracted image of diffractions corresponding to 1420 m/s migration velocity after applying velocity continuation method on the diffraction data. Notice the concave down (circled) diffraction response at the sea floor. The migration velocity at sea floor is expected to be around 1500 m/s, thus migrating with a lower velocity (1420 m/s) causes diffractions to concave down.

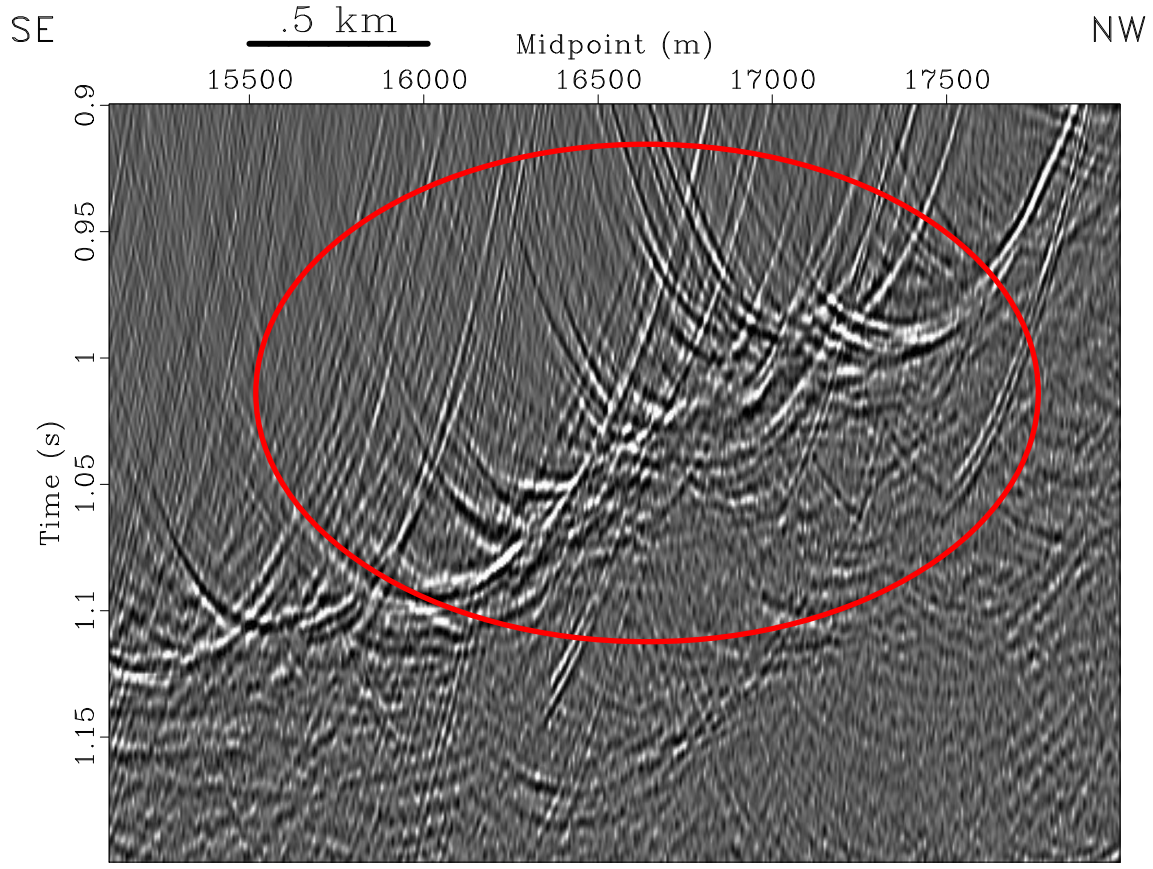

Figure 5.4: Extracted image of diffractions corresponding to 2500 m/s migration velocity after applying velocity continuation method on the diffraction data. Notice the concave up (circled) diffraction response at the sea floor. The migration velocity at sea floor is expected to be around 1500 m/s, thus migrating with a higher velocity (2500 m/s) causes diffractions to concave down. Compare the resutls from this figure with ones from Figure 5.3.

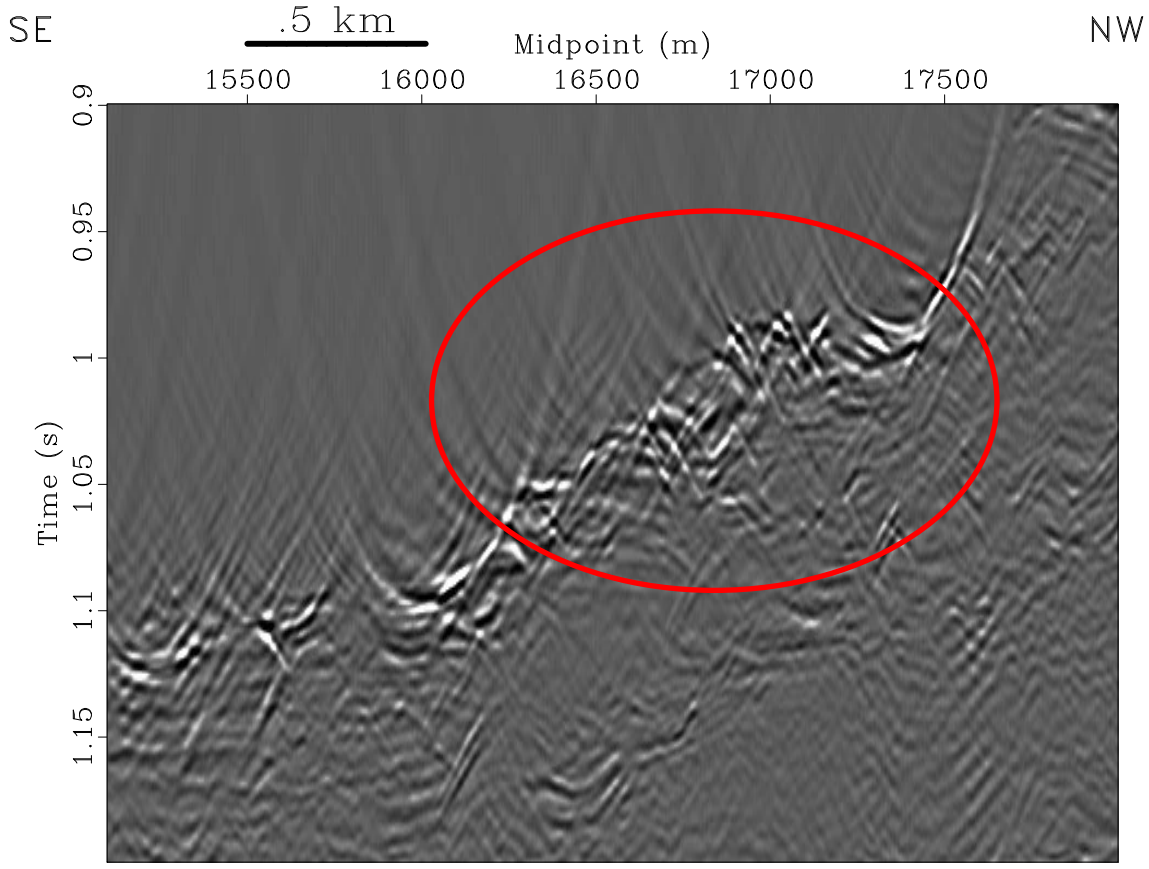

Figure 5.5: Integral-path diffraction image generated by summing the 201 diffraction images obtained via velocity continuation method. Notice that the sea floor diffractions tails tend to focus into their apexes. Curvatures of diffraction decreases as migration velocity approximates the correct one. Therefore, summing the diffraction images created by different velocities destroys the tails of diffractions while presering their apexes.

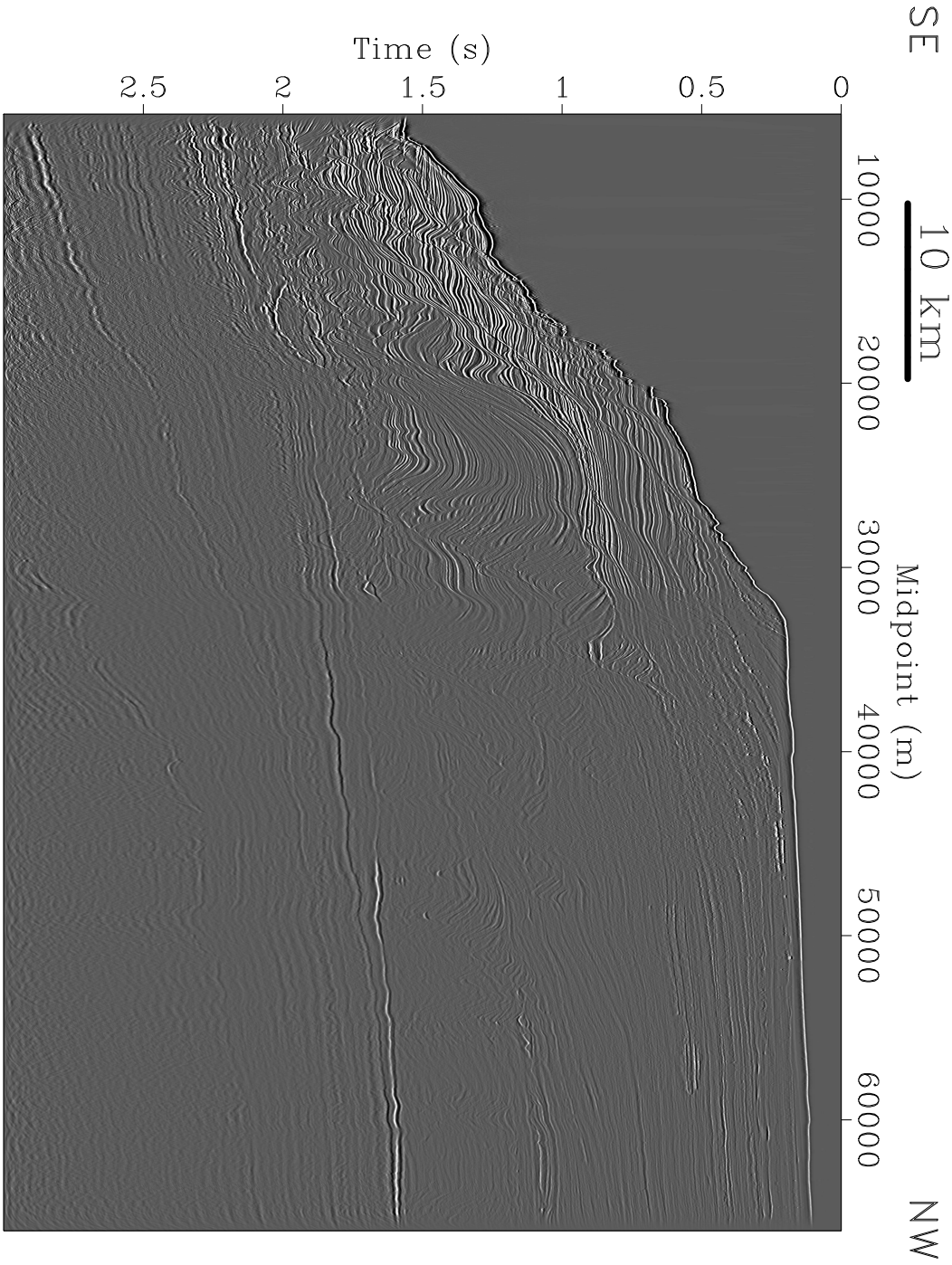

Figure 5.6: Conventional image of Line 12. Notice the area corresponding to mounded reflection energy on the left of the figure.

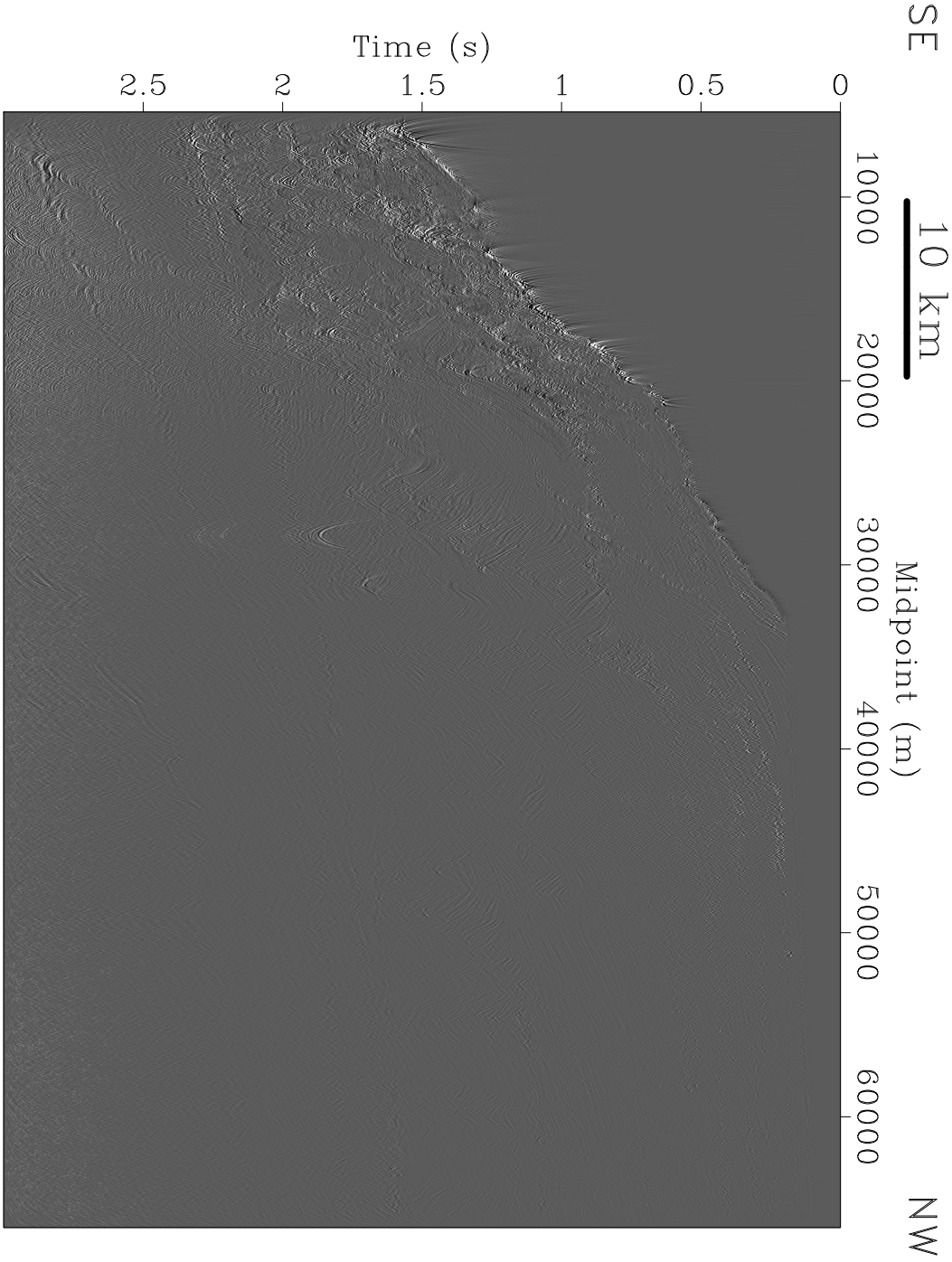

Figure 5.7: Diffraction image of Line 12. The small diffracting and energy scaterer objects appear on the left of the figure. The area is above the mounded reflection energy observed in the conventional image.

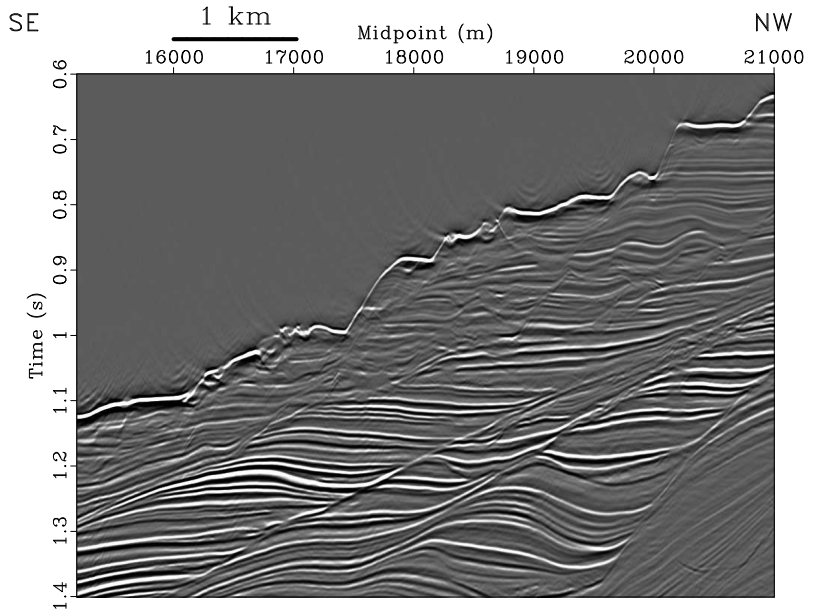

(a)

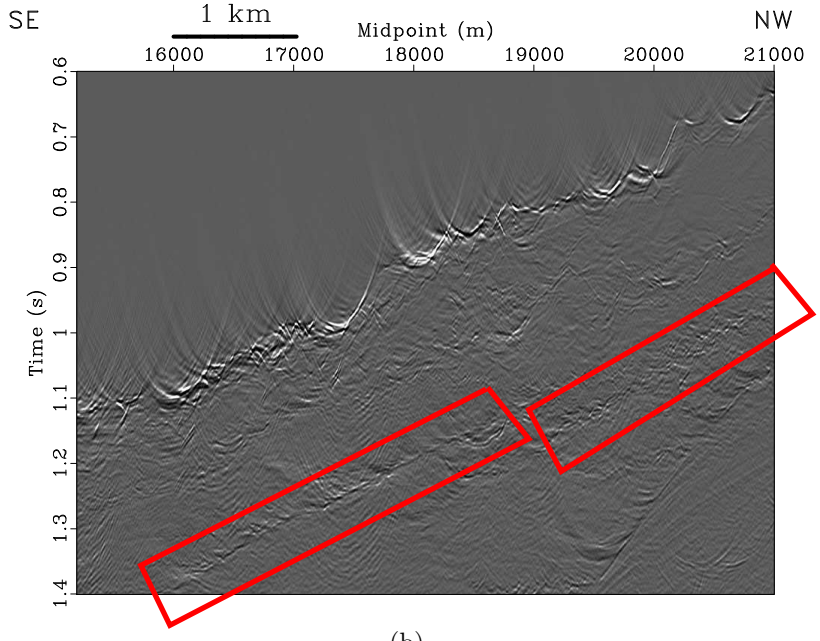

(b)

Figure 5.8: Conventional image (a). The corresponding diffraction image (b). Note the enhancements of the fault locations in (b)

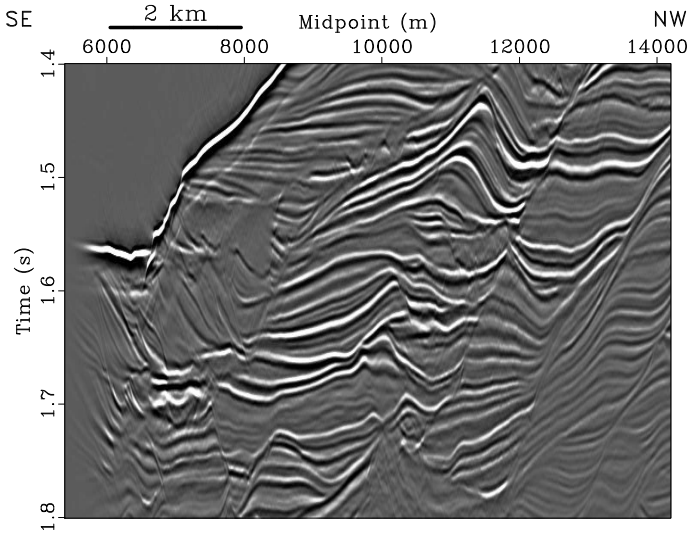

(a)

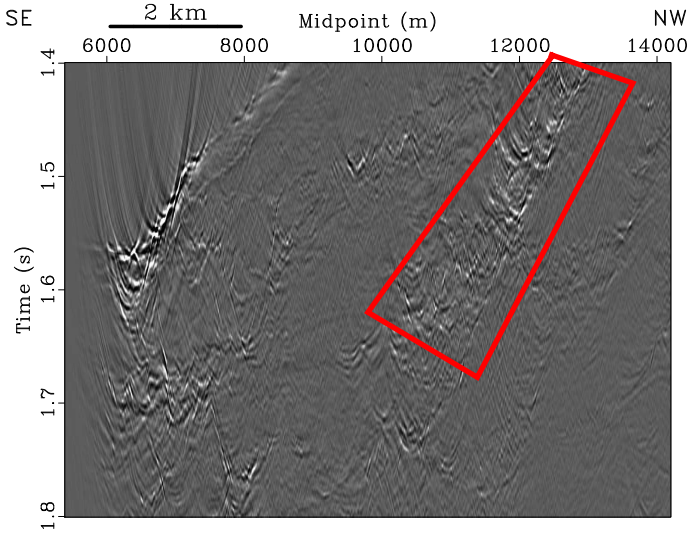

(b)

Figure 5.9: Conventional image (a) and its corresponding diffraction image (b) for another portion of the Line 12.

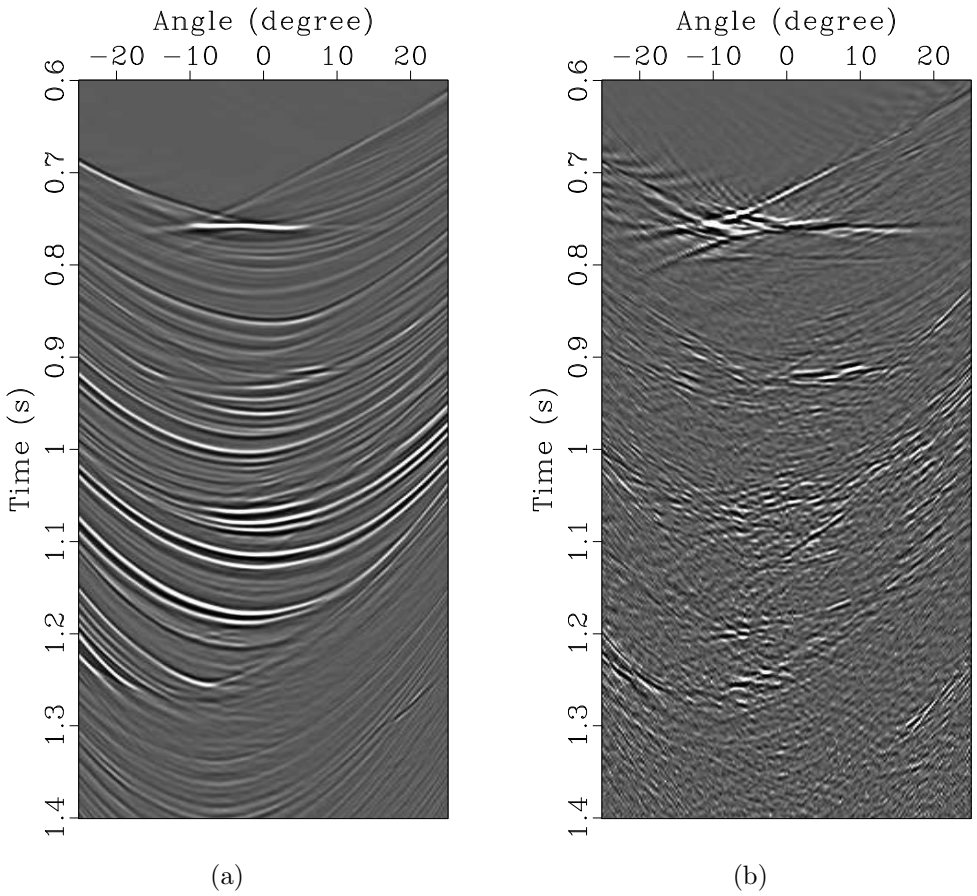

Figure 5.10: dip-angle gather from conventional image gathers (a) extracted from the migrated DMO stack using Kirchhoff migration in the dip-angle gather domain. The corresponding dip-angle gather (b) from diffraction image gathers. Notice the different geometrical characteristics of diffractions and reflections in the left figure. Diffractions appear weak and tend to be flat (circled) while reflections appear strong and concave-up. Also note that after diffraction separation (right figure), the diffraction energy is enhanced.

Discussion

Combining diffraction data with velocity continuation and path-integral is a promising migration velocity analysis method. Velocity continuation produces, according to mathematical descriptions, several images of diffraction data where each image produced with a different constant velocity. Diffractions in those images can be: over-migrated (concave up) or under-migrated (concave down) or focused in their apexes. Velocity continuation, which is a time migration process, is affected by the velocity increment in each step and the range of velocities.

Integral-path method (Burnett and Fomel, 2011) is based on the assumption that diffraction apexes are stationary points and do not change regardless of migration velocity used. Based on this assumption, summing the images should ideally destroy under and over migrated diffractions while preserving the focused diffraction. The results from integral path method, however, can be undermined by residual reflection data, as shown in Figure 5.5. One may need to use stacking velocities to constrain the range of migration velocities during the summation process.

Chapter 6

Conclusions

Summary

The goal of diffraction imaging is to extract and focus diffraction energy that describes the location of diffractors present in the subsurface. Significanlty, the focusing of diffractions provides a tool for migration velocities analysis. The estimated migration velocity then can be used to obtain both a diffraction image and an enhanced conventional image. The extracted diffraction image for seismic 2D Line 12 from the Canterbury Basin, New Zealand reveals subtle details about the geology of the subsurface which are hidden in the conventional image. In particular, the diffraction image illuminated the locations of small-scale faults and further exposed unconformities present in the sediment drifts. Both the extracted diffraction and enhanced conventional images enable interpreters to characterize the subtle details of the sediment drifts in the Canterbury Basin.

In summation, I began by describing the geology of the Canterbury Basin. Then, I reviewed the three fundamental seismic data processing steps: deconvolution, stacking, and migration. This was followed by a review of the supportive secondary processes such as filtering and amplitude gain. Next, SRME was applied to predict multiple energy, and applied regularized non-stationary regressions to adaptively subtract the predicted multiples. After that, I suppressed reflection energy using PWD method for the DMO stack. Next the separated diffractions stack was

used to estimate migration velocities using velocity continuation and integral-path methods. Both a conventional migrated section and a diffraction migrated section were produced using Kirchhoff migration in the dip-angle gather domain.

In addition, I reproduced synthetic data models from the literature and created additional models as well. These synthetic models tested theories used in this thesis and also explain the results obtained from processing the field dataset. For one example, the importance of using DMO stack for diffraction imaging was clearly explained. For another example, reproducing the graben and syncline model in Chapter 3 demonstrated that applying diffraction imaging may allow one to observe the diffraction seismic response from reflectors with small radii of curvature. These synthetic models demonstrated theories and illustrated their application on field dataset.

Applying diffraction imaging with a similar processing workflow on the remaining Canterbury Basin datasets from New Zealand may reveal more details about the subsurface and the 3D nature of the sediment drifts. The processing steps applied to Line 12 are reproducible and were achieved using the Madagascar software package. Madagascar is an open-source software processing package that supports reproducible research and provides a framework to verify theory using synthetic data and process field data as well. One may easily modify the processing instructions available in Madagascar to work for other datasets from the Canterbury Basin.

Possible future work that could be applied to the Canterbury dataset is the combined method of diffraction imaging, as demonstrated recently by Klokov and Fomel (2012). They first suppress a part of the reflection energy using plane-wave destruction method. The PWD method, which is a data-driven separation, can be applied to post-stack data or prestack data (zero-offset, or multi-offset gathers). The

separated dataset which should contain diffractions and residual reflections are then migrated in the dip-angle gather domain. In this domain, reflections and diffractions have different geometrical shapes. By viewing one dip-angle gather directly above a diffractor, the reflections have smiley shapes (approximated hyperbolas) while the diffractions appear flat. With this observation, diffractions are enhanced by further separation applied using Hybrid Radon transform.

Another possible future research topic would be to investigate whether the PWD method also suppresses multiple reflection energy during diffractions separation step. Multiple reflections in the offset domain resemble primary reflections - smooth laterally continuous events. Intuitively, local slope estimation using PWD should suppress both primary and multiple reflection energy. One thus may obtain diffraction images without going through the complicated reflection multiple attenuation steps. However, other kinds of multiple energy such as diffracted multiple energy may be present in the obtained diffraction image.

Bibliography

Biondi, B. L., 2006, 3d seismic imaging: Society of Exploration Geophysicists.

Bishop, K., J. Keliher, J. Paffenholz, D. Stoughton, S. Michell, R. Ergas, and M. Hadidi, 2001, Investigation of vendor demultiple technology for complex subsalt geology: SEG Technical Program Expanded Abstracts, **20**, 1273–1276.

Burnett, W., and S. Fomel, 2011, Azimuthally anisotropic 3D velocity continuation: International Journal of Geophysics, Accepted for publication.

Burnett, W., S. Fomel, and R. Bansal, 2011, Diffraction velocity analysis by path-integral seismic imaging: SEG Technical Program Expanded Abstracts, **30**, 3898–3902.

Claerbout, J. F., 1971, Toward a unified theory of reflector mapping: Geophysics, **36**, 467–481.

———, 1985, Imagining the earth's interior: Blackwell Science.

———, 1992, Earth soundings analysis: Processing versus inversion: Blackwell Science.

Claerbout, J. F., and S. M. Doherty, 1972, Downward continuation of moveout-corrected seismograms: Geophysics, **37**, 741–768.

Dragoset, W., and v. Jeričević, 1998, Some remarks on surface multiple attenuation: Geophysics, **63**, 772–789.

Faugres, J.-C., and D. A. Stow, 1993, Bottom-current-controlled sedimentation: a synthesis of the contourite problem: Sedimentary Geology, **82**, 287 – 297.

Fomel, S., 1994, Method of velocity continuation in the problem of temporal seismic migration: Russian Geology and Geophysics, **35**, 100–111.

———, 2002, Applications of plane-wave destruction filters: Geophysics, **67**, 1946–1960.

———, 2003, Time-migration velocity analysis by velocity continuation: Geophysics, **68**, 1662–1672.

———, 2007, Velocity-independent time-domain seismic imaging using local event slopes: Geophysics, **72**, S139–S147.

———, 2009a, Adaptive multiple subtraction using regularized nonstationary regression: Geophysics, **74**, V25–V33.

———, 2009b, Velocity analysis using ab semblance: Geophysical Prospecting, **57**, 311–321.

Fomel, S., E. Landa, and M. T. Taner, 2007, Poststack velocity analysis by separation and imaging of seismic diffractions: Geophysics, **72**, U89–U94.

Fomel, S., and M. Prucha, 1999, Angle-gather time migration: SEP-Report, **100**, 141–150.

Foster, D. J., and C. C. Mosher, 1990, Multiple suppression using curvilinear radon transforms: SEG Technical Program Expanded Abstracts, **9**, 1759–1759.

Gersztenkorn, A., and K. J. Marfurt, 1999, Eigenstructure-based coherence computations as an aid to 3-d structural and stratigraphic mapping: Geophysics, **64**, 1468–1479.

Hale, D., 1991, Dip moveout processing?: Society of Exploration Geophysicists.

Hampson, D., 1986, Inverse velocity stacking for multiple elimination: J. Can. Soc. Expl. Geophys, **22**, 44–55.

Harlan, W. S., J. F. Claerbout, and F. Rocca, 1984, Signal/noise separation and velocity estimation: Geophysics, **49**, 1869–1880.

Khaidukov, V., E. Landa, and T. J. Moser, 2004, Diffraction imaging by focusing-defocusing: An outlook on seismic superresolution: Geophysics, **69**, 1478–1490.

Klem-Musatov, K., 1994, Theory of seismic diffractions: Soc. of Expl. Geophys. (Edited by Hron Fronta and Larry Lines).

Klokov, A., R. Baina, and E. Landa, 2010, Separation and imaging of seismic diffractions in dip angle domain: EAGE Conference Barcelona, Extended Abstracts.

Klokov, A., and S. Fomel, 2012, Separation, imaging, and velocity analysis of seismic diffractoins using migrated dip-angle gathers: Geophysics, **submitted**.

Landa, E., 2004, Imaging without a velocity model using path-summation approach: SEG Technical Program Expanded Abstracts, **23**, 1818–1821.

———, 2009, Beyond Conventional Seismic Imaging: EAGE.

Landa, E., S. Fomel, and T. Moser, 2006, Path-integral seismic imaging: Geophysical Prospecting, **54**, 491–503.

Landa, E., S. Fomel, and M. Reshef, 2008, Separation, imaging, and velocity analysis of seismic diffractions using migrated dip-angle gathers: SEG Technical Program Expanded Abstracts, **27**, 2176–2180.

Landa, E., V. Shtivelman, and B. Gelchinsky, 1987, A method for detection of diffracted waves on common-offset sections: Geophysical Prospecting, **35**, 359–373.

Lu, H., and C. S. Fulthorpe, November/December, 2004, Controls on sequence stratigraphy of a middle miocenеholocene, current-swept, passive margin: Offshore canterbury basin, new zealand: Geological Society of America Bulletin, **116**, 1345–1366.

Lu, H., C. S. Fulthorpe, and P. Mann, 2003, Three-dimensional architecture of shelf-building sediment drifts in the offshore canterbury basin, new zealand: Marine Geology, **193**, 19 – 47.

Lu, H., C. S. Fulthorpe, P. Mann, and M. A. Kominz, 2005, Miocenerecent tectonic

and climatic controls on sediment supply and sequence stratigraphy: Canterbury basin, new zealand: Basin Research, **17**, 311–328.

Margrave, G. F., 1998, Theory of nonstationary linear filtering in the fourier domain with application to time-variant filtering: Geophysics, **63**, 244–259.

Moser, T., and C. Howard, 2008, Diffraction imaging in depth: Geophysical Prospecting, **56**, 627–641.

Prucha, M. L., B. L. Biondi, and W. W. Symes, 1999, Angle-domain common image gathers by wave-equation migration: SEG Technical Program Expanded Abstracts, **18**, 824–827.

Reshef, M., and E. Landa, 2009, Post-stack velocity analysis in the dip-angle domain using diffractions: Geophysical Prospecting, **57**, 811–821.

Robinson, E. A., and S. Treitel, 2000, Geophysical signal analysis: Society of Exploration Geophysicists.

Sava, P., and A. Guitton, 2005, Multiple attenuation in the image space: Geophysics, **70**, V10–V20.

Sava, P. C., B. Biondi, and J. Etgen, 2005, Wave-equation migration velocity analysis by focusing diffractions and reflections: Geophysics, **70**, U19–U27.

Schneider, W. A., 1978, Integral formulation for migration in two and three dimensions: Geophysics, **43**, 49–76.

Sheriff, R. E., 2002, Encyclopedic dictionary of applied geophysics, fourth ed.: Society of Exploration Geophysicists.

Stoffa, P. L., 1989, Tau-p: a plane wave approach to the analysis of seismic data: Kluwer Academics Publishers.

Trorey, A. W., 1970, A simple theory for seismic diffractions: Geophysics, **35**, 762–784.

Verschuur, D. J., A. J. Berkhout, and C. P. A. Wapenaar, 1992, Adaptive surface-related multiple elimination: Geophysics, **57**, 1166–1177.

Weglein, A. B., 1999, Multiple attenuation: an overview of recent advances and the road ahead (1999): The Leading Edge, **18**, 40–44.

Yilmaz, 2001, Seismic data analysis: Society of Exploration Geophysicists.